

Mitochondrial transfer from MSCs to T cells induces Treg differentiation and restricts inflammatory response

Angela C Court^{1,2,†}, Alice Le-Gatt^{1,†}, Patricia Luz-Crawford^{2,†} , Eliseo Parra³, Victor Aliaga-Tobar^{4,5}, Luis Federico Bádiz², Rafael A Contreras², María Ignacia Ortúzar¹, Mónica Kurte², Roberto Elizondo-Vega², Vinicius Maracaja-Coutinho^{4,5}, Karina Pino-Lagos², Fernando E Figueroa^{2,3,*}  & Maroun Khoury^{1,2,3,6,**} 

Abstract

Mesenchymal stem cells (MSCs) have fueled ample translation for the treatment of immune-mediated diseases. They exert immunoregulatory and tissue-restoring effects. MSC-mediated transfer of mitochondria (MitoT) has been demonstrated to rescue target organs from tissue damage, yet the mechanism remains to be fully resolved. Therefore, we explored the effect of MitoT on lymphoid cells. Here, we describe dose-dependent MitoT from mitochondria-labeled MSCs mainly to CD4⁺ T cells, rather than CD8⁺ T cells or CD19⁺ B cells. Artificial transfer of isolated MSC-derived mitochondria increases the expression of mRNA transcripts involved in T-cell activation and T regulatory cell differentiation including FOXP3, IL2RA, CTLA4, and TGFβ1, leading to an increase in a highly suppressive CD25⁺FoxP3⁺ population. In a GVHD mouse model, transplantation of MitoT-induced human T cells leads to significant improvement in survival and reduction in tissue damage and organ T CD4⁺, CD8⁺, and IFN-γ⁺ expressing cell infiltration. These findings point to a unique CD4⁺ T-cell reprogramming mechanism with pre-clinical proof-of-concept data that pave the way for the exploration of organelle-based therapies in immune diseases.

Keywords graft-versus-host disease; immunosuppression; mesenchymal stem cells; mitochondrial transfer; T regulatory cells

Subject Categories Immunology; Molecular Biology of Disease; Stem Cells & Regenerative Medicine

DOI 10.15252/embr.201948052 | Received 7 March 2019 | Revised 11

November 2019 | Accepted 29 November 2019

EMBO Reports (2020) e48052

Introduction

Mitochondria (MT) are the key players of energy balance and cell metabolism, and several lines of evidence indicate that the functional state of immunocompetent cells runs parallel to their metabolic condition [1]. Indeed, mitochondrial degradation, biogenesis, and network formation are fundamental processes related to the metabolic control of T-cell function *in vivo* [2]. A recently studied phenomenon that contributes to mitochondrial dynamics is the intercellular transfer of MT between different cell types. Such cell-to-cell mitochondria mitochondria (MitoT) was first demonstrated for human mesenchymal stem cells (MSCs). These were able to rescue the growth of MT-deficient cancer cells by the transfer of their own healthy MT, reinstating the target cell mitochondrial network [3]. MSCs are known to exert tissue-restoring and immunosuppressive effects that have been clinically tested for the treatment of inflammatory or immune-mediated diseases including graft-versus-host disease (GVHD) [4]. The significance of MitoT *in vivo* has been established in airway disease models in which the intra-tracheal administration of MSCs was associated with the transfer of MT to alveolar epithelium, triggering an increase in metabolic activity while improving lung damage and disease outcome in the treated animals [5]. Jackson *et al* [6] observed that MT transferred from MSCs were able to increase the phagocytic capabilities of macrophages, also in a murine model of respiratory disease; however, the MitoT to other immunocompetent cells has not been addressed. In this regard, a recent technique named “Mitoception” by Caicedo *et al* describes an artificial procedure to transfer MT from a donor into recipient cells. They demonstrated that freshly isolated MT from MSCs could be transferred into a cancer cell line based on

1 Cells for Cells, Santiago, Chile

2 Centro de Investigación Biomédica, Faculty of Medicine, Universidad de los Andes, Santiago, Chile

3 Laboratory of Nano-Regenerative Medicine, Faculty of Medicine, Universidad de los Andes, Santiago, Chile

4 Centro de Modelamiento Molecular, Biofísica y Bioinformática (CM²B²), Facultad de Ciencias Químicas y Farmacéuticas, Universidad de Chile, Santiago, Chile

5 Advanced Center for Chronic Diseases – ACCDiS, Facultad de Ciencias Químicas y Farmacéuticas, Universidad de Chile, Santiago, Chile

6 Consorcio Regenero, Chilean Consortium for Regenerative Medicine, Santiago, Chile

*Corresponding author. Tel: +56 2 226181455; E-mail: ffigueroa@uandes.cl

**Corresponding author. Tel: +56 2 226181956; E-mail: mkhoury@uandes.cl

†First co-authors

centrifugation and endocytosis. The “mitocepted” cells were able to increase their ATP production while shifting toward a glycolytic pathway [7]. Thus, the process of Mitoception allows a distinct analysis of the functional role of MT, independently from the paracrine and cell-mediated effects that MSCs are known to exert on their target cells.

We hypothesized that MitoT can target immunocompetent cells and play a role in the regulation of T-cell function, contributing to the dampening of inflammation that is associated with MSC therapy. Herein, we provide evidence of MitoT to human T-cell subpopulations, assessing functional, transcriptomic, and metabolic effects on cell function *in vitro* and in an animal model of GVHD *in vivo*. These findings unravel a unique mechanism involved in the control of immune-mediated diseases by cell and organelle therapies, through physiological and artificial MitoT from MSCs to lymphocytes.

Results

Rapid and dose-dependent transfer of MT from MSCs to PBMC *in vitro*

To explore the MitoT from MSCs to human immune cells, donor cells were labeled with MT-specific fluorescent probe (MitoTracker Green) and then co-cultured with human PBMCs (Fig 1A). Immunofluorescent imaging revealed MSC-MT in PBMCs (Fig 1B). MitoT to specific populations of immunocompetent cells was then assessed by flow cytometry (FACS), finding that ~40% of CD45⁺ cells acquired MitoTracker stain, even from different donors and varying sources of labeled MSC-derived MT (Fig 1C and Table EV1), confirming that this property was extensive to all tested MSCs. Similarly, using subpopulation-specific antibodies, we were able to evidence MitoT to CD3⁺ T, CD19⁺ B, and CD56⁺ natural

killer (NK) cells (Figs 1D and EV1A and B), mainly directed to T-helper CD4⁺ (57%) rather than T cytotoxic CD8⁺ lymphocytes (19%; $P = 0.0008$; Fig 1E). A dose–response curve of MitoT was observed within the CD45⁺CD3⁺ gated population when donor MSCs were co-cultured at increasing MSC:PBMC ratios (1:100, 1:25, and 1:10), with an average of 9.3, 32.7, and 40.0% positivity for MT label, respectively (Fig 1F and G; $P < 0.0001$). These results provided the setting conditions we chose for the ensuing experiments. To further characterize the time kinetics of MitoT, similar conditions were evaluated at 24, 48, and 72 h, with no differences noted with longer incubation times (Fig EV1C). Surprisingly, with shortened time point experiments, MitoT was detected within 1 h, peaking at only 5 h of co-culture (2.2 and 36.7% of T CD3⁺ MitoT^{pos} cells, respectively; Figs 1H and EV1D and E). This reflects the very short time required for the transfer process. The inhibition of MitoT at 4°C and the lack of MitoT^{pos} CD3⁺ T cells when supernatant from labeled MSCs was used (Fig EV1F) point to the mediation of an energy-dependent process, not attributable to passive transfer due to unspecific signals such as dye leakage of the MitoTracker. Furthermore, a negligible amount of MitoT was observed from PBMCs to MSCs, and no detection of MitoT was observed from MSCs to MSCs (Fig EV1G and H), pointing to a target-specific and unidirectional MT transfer. To reinforce the occurrence of MitoT, we quantified the mean fluorescent intensity (MFI) of MitoTracker-labeled MSCs at baseline and after PBMCs co-culture, evidencing a significant 3.6-fold decrease in the mitochondrial fluorescent signal in MSCs post-co-culture ($P = 0.0003$), confirming the loss of the signal as result of the MT donation (Fig 1I). MitoT was confirmed by confocal microscopy, which showed the presence of labeled umbilical cord (UC)-MSC-derived MT inside the co-cultured human CD3⁺ T cells stained in red (Fig 1J). Using human–mouse cell co-culture experiments, we validated MitoT from MSCs by qPCR, as only mitochondrial-specific human gene expression was detected, with no human B2M expression in FACS-sorted mouse

Figure 1. MSCs efficiently transfer mitochondria in a dose-dependent manner to T and B lymphocytes.

- A Schematic representation of the experimental design used for co-culture experiments.
- B Representative confocal microscopy of human PBMCs stained with DAPI (white arrows) co-cultured with previously labeled UC-MSC with MitoTracker-Green (top image) and specific antibody for human CD90 (bottom image).
- C Percentage of mitochondrial transfer (MitoT) on total human CD45⁺ cells after 24 h co-culture with MitoTracker-Green labeled bone marrow (BM), menstrual (Mens) or umbilical cord (UC)-MSCs (MSC:PBMC ratio 1:25) ($n = 3$ biological replicates, with three different donors of BM, Mens and UC-MSCs).
- D FACS analysis of MitoT on T CD3⁺ ($n = 4$), B CD19⁺ ($n = 4$) and natural killer (NK) CD56⁺ ($n = 3$) cells after 24 h co-culture with MitoGreen labeled UC-MSCs (ratio 1:25) (Biological replicates, with different donors of UC-MSCs).
- E FACS analysis of MitoT on CD3⁺ CD4⁺ or CD3⁺ CD8⁺ T cell populations after 24 h co-culture with labeled UC-MSCs (ratio 1:25) ($n = 3$ biological replicates, with three different donors of UC-MSCs).
- F Representative FACS plots of MitoT on CD45⁺ CD3⁺ T cells at increasing amounts of UC-MSC.
- G Percentage of MitoT on CD45⁺ CD3⁺ human cells after 24 h co-culture with increasing ratios of UC-MSC:PBMCs ($n = 5$ biological replicates, with five different UC-MSCs and 5 different PBMCs).
- H FACS analysis of MitoT on CD45⁺ CD3⁺ T cells after short times of co-culture with UC-MSCs at two different temperatures, at a ratio 1:25 ($n = 3$ biological replicates, with three different UC-MSCs and three different PBMCs).
- I Mean fluorescence intensity (MFI) of MitoTracker-Green+ UC-MSCs at baseline or after 72 h PBMC co-culture. Representative FACS plot (left panel) and average of MFI ($n = 4$ biological replicates, with four different UC-MSCs) (right panel).
- J Confocal microscopy of human PBMCs after co-culture with MitoTracker-Green stained UC-MSCs. Images showed MSC-mitochondria (green) inside the CD3⁺ T cells (red).
- K qPCR analysis of human β -microglobulin (B2M), human specific mitochondrial (Mito) and mouse specific (β -actin) gene expression levels in UC-MSCs, mouse derived spleen cells or FACS sorted CD45⁺ mouse cells after 24 h co-culture with UC-MSCs ($n = 3$ biological replicates). n/d = not detected.
- L *In vivo* experimental design for MitoT in Balb/c mice transplanted with MitoTracker Green labeled MSCs.
- M FACS analysis of *in vivo* MitoT from UC-MSCs to Balb/c mouse mesenteric lymph node and spleen cells, 24 h after intraperitoneal transplantation of 5×10^6 MitoTracker-labeled MSCs or without cells (control) ($n = 1$).

Data information: In (C–E, G–I and K), graphs show mean \pm SEM and statistical analysis by Student's *t*-test.

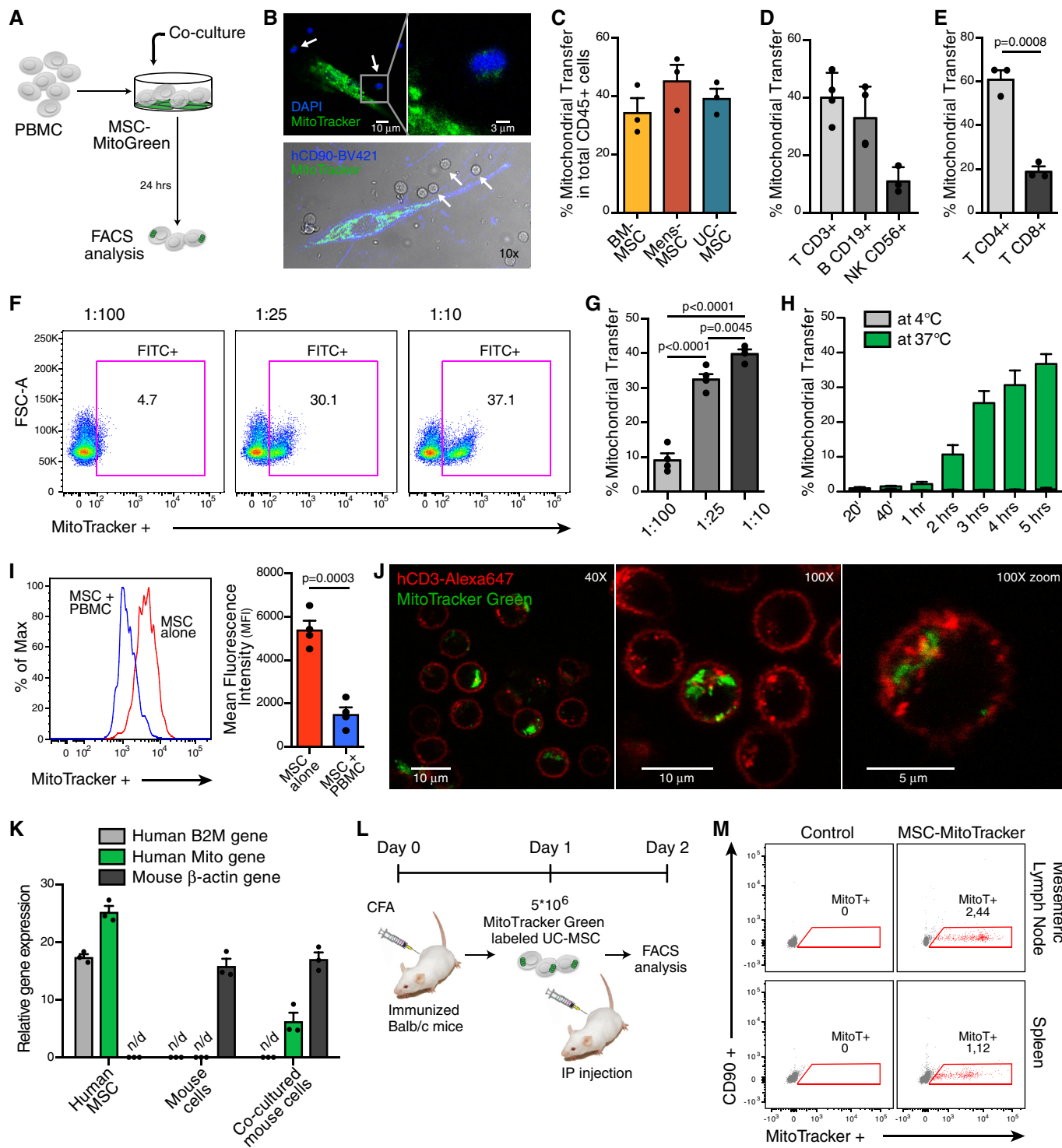


Figure 1.

splenoocytes previously co-cultured with UC-MSCs (Fig 1K). This confirmed that organelle transfer is not attributable to cell fusion. Since in non-lymphoid cells MitoT has been previously shown to occur in response to target cell oxidative stress or damage [5] and MSC effects are activated by inflammatory signaling [8], we tested the effect of target cell conditions on MitoT, finding that

anti-oxidant treatment with pterostilbene did not modulate MitoT from MSCs to human CD3⁺ T cells (Fig EV11), as neither did prior MSC licensing with IFN- γ and IL1 β (Fig EV1J).

Finally, to corroborate that MSCs exert MitoT to lymphocytes also *in vivo*, experiments were designed using Balb/c mice previously immunized with Complete Freund's Adjuvant (CFA) and

transplanted with MitoTracker-labeled UC-MSCs (Fig 1L). Mouse mesenteric lymph nodes and spleen cells were harvested after 24 h and flow cytometry analysis, gating on total leukocyte population, showed a 2.4 and 1.12% positivity for MitoTracker label, respectively, substantiating that MSCs are capable of *in vivo* MitoT (Fig 1M).

CD3⁺ T cells are permissive to artificial mitochondrial transfer

Artificial MitoT referred as “Mitoception” was used to selectively assess the functional impact that MitoT from UC-MSCs had on T cells, independently from the effects due to cell contact or other paracrine factors. On that ground, functional and biologically active MT were isolated from UC-MSCs and incubated with human PBMCs following the Mitoception protocol [7] (Fig 2A). As visualized by confocal microscopy images and flow cytometry, isolated MSC-MT displayed a physiological mitochondrial membrane potential (MMP) as revealed by MitoTracker Red CMXRos and TMRM-positive stains (Fig EV2A–C). Further activity of isolated MSC-MT was assessed by measurements of ATP production (Fig EV2D), demonstrating that the MT we transferred to T cells were active and functional. Confocal microscopy images revealed the presence of both endogenous and exogenous MT (labeled with MitoTracker

Red and MitoTracker Green, respectively) within the target CD3⁺ T cells (Fig 2B). CD3⁺ T cells were permissive to artificial MitoT mimicking the co-culture condition, since a dose-dependent uptake of MSC-derived MT equivalent to MSC:PBMC ratios of 1:100, 1:25, and 1:10 was evidenced, with an average of 15, 36, and 50.4% of MitoTracker-labeled CD3⁺ T cells, respectively (Fig 2C). Also, using transmission electron microscopy, a significant twofold increase in MT numbers was counted in the sorted CD3⁺ MitoT^{pos} target cells compared with MitoT^{neg} cells (average of 11 and 5 per cell, respectively, $P < 0.0001$; Fig 2D and E); nevertheless, no changes on area, length, or MT perimeter were observed between both groups (Fig EV2E). To determine the status of the mitochondrial dynamics within the CD3⁺ MitoT^{pos} cells, we evaluated fusion/fission key players mRNA levels and protein expression changes. After 48 h post-mitoception, a significant reduction in Opa1, Mfn1/2, and Dnm1l mRNA expression was observed when comparing CD3⁺ MitoT^{pos} and MitoT^{neg} cells, although no significant differences were observed in protein levels at the evaluated times points (Fig EV2F and G). Phosphorylated Ser616-DRP1 (p-DRP1) was not detected.

Metabolic activity changes were measured using extracellular flux analysis on sorted CD3⁺ MitoT^{pos} and CD3⁺ MitoT^{neg} cells. The extracellular acidification rate (ECAR), indicative of the

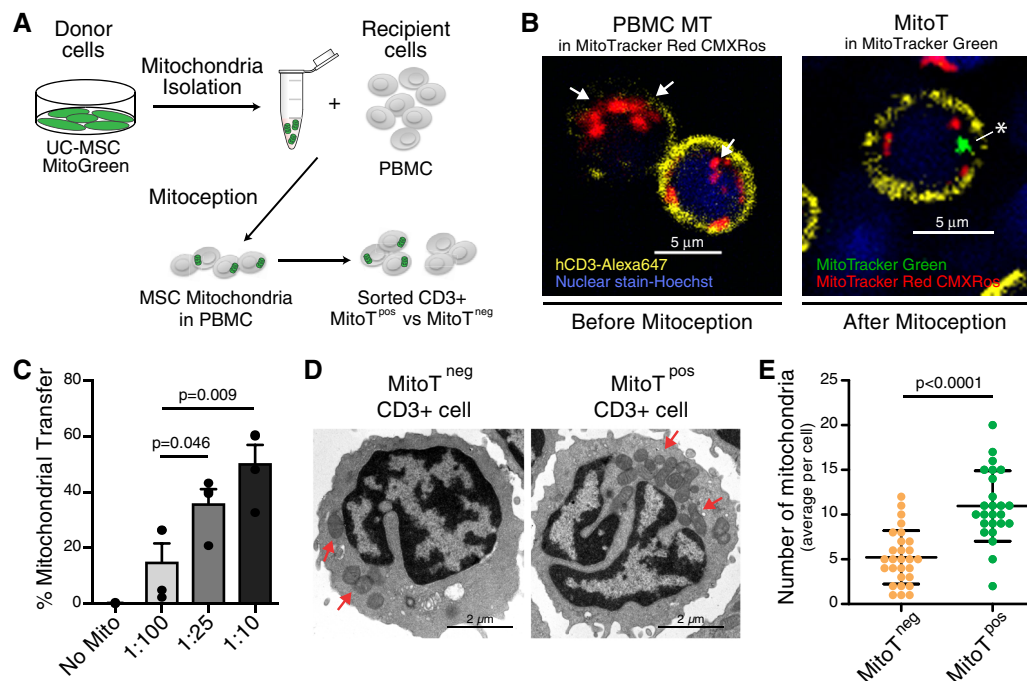


Figure 2. CD3⁺ T cells are permissive to artificial MitoT (Mitoception) resulting in an increase of their mitochondrial content.

- A Schematic representation of the experimental design of the Mitoception protocol.
- B Confocal microscopy images of human CD3⁺ T cells with endogenous MT-labeled with MitoTracker Red CMXRos (white arrows, left panel) or after Mitoception with MitoTracker Green labeled-MT from UC-MSCs (white asterisk, right panel).
- C FACS analysis of MitoT on CD3⁺ human T cells after Mitoception with increasing amounts of UC-MSC-MT corresponding to the same cell number ratios used in co-culture experiments ($n = 4$ biological replicates, with 4 different donors of UC-MSCs). Graph shows mean \pm SEM and statistical analysis by Student's *t*-test.
- D Representative transmission electron microscopy images of FACS-sorted human CD3⁺ MitoT^{neg} and CD3⁺ MitoT^{pos} cells following Mitoception with UC-MSC-MT. Red arrows show human mitochondria.
- E Quantification of human MT in sorted CD3⁺ MitoT^{neg} and MitoT^{pos} cells after Mitoception with UC-MSCs, by transmission electron microscopy ($n = 25$ independent cells analyzed per group). Graph shows mean \pm SEM and statistical analysis by Student's *t*-test.

glycolytic activity, showed a significant 1.6-fold increase in the basal glycolysis (measured as ECAR above basal after adding glucose) in MitoT^{pos} compared with MitoT^{neg} cells ($P < 0.0001$; Fig EV3A and B), but no changes were observed for glycolytic capacity (measured as maximal ECAR above basal after ATP synthase inhibition with oligomycin; Fig EV3C). In contrast, the oxygen consumption rate (OCR, an indicator of OXPHOS activity) did not show any variation of the basal mitochondrial respiration (measured as basal OCR before ATP synthase inhibition with oligomycin) between MitoT^{pos} and MitoT^{neg} cells, though a significant decrease in the maximum respiration was observed (measured as OCR above basal after uncoupling with FCCP) in MitoT^{pos} cells in comparison with MitoT^{neg} cells ($P = 0.04$; Fig EV3D–F), which is linked to the capacity of the cells to adapt to a stressful environment or increased work conditions. Moreover, using the ECAR/OCR ratio, a significant 1.5-fold increase ($P = 0.011$) was computed for the mitocepted T-cell population, suggesting a metabolic switch toward an activated state of the lymphocyte population (Fig EV3G), even though lactate production remained the same between CD3⁺ MitoT^{pos} compared with CD3⁺ MitoT^{neg} cells (Fig EV3H).

Transmigration capacity of MSC-mitocepted T cells was also analyzed using a commercial Transwell device. After 4 h of incubation, FACS-sorted CD4⁺ MitoT^{pos} cells that were activated with anti-CD3 and IL-2 showed a significant increase in migration capacity compared with MitoT^{neg} cells ($P = 0.0087$, Fig EV3I). Functional analysis showed no differences in the proliferation rate of mitocepted CD3⁺ T cells compared with control conditions (Fig EV3J and K).

MitoT induces changes in mRNA expression associated with T-cell activation pathways

To further assess the functional impact of exogenous MSC-derived MT on human T-cell function, we performed whole transcriptome RNA sequencing (RNA-Seq) of FACS-sorted CD3⁺ MitoT^{pos} and CD3⁺ MitoT^{neg} cells. Differential gene expression (using HISAT2 software version 2.0.5) was first analyzed finding 191 coding genes that were differentially expressed (DE; at FDR 5%) between MitoT^{pos} as opposed to MitoT^{neg} CD3⁺ cells (Fig 3A). Volcano plots depict DE genes that were upregulated or downregulated in response to MitoT (Fig 3B). Unsupervised hierarchical clustering, as heat map representation, performed for all coding DE genes, revealed that T-cell regulation and/or activation-related gene

expression distinguished MitoT^{pos} from MitoT^{neg} CD3⁺ sorted samples (Figs 3C and EV4A). Further gene set enrichment analysis (GSEA) of RNA-Seq data revealed over-representation of modules containing genes related to functional pathways including MT membrane organization and biogenesis and co-expression/interaction network displaying *FOXP3* as hub gene (Fig EV4B–D). Next, to elucidate the roles of the DE genes we used the web-based Enrichr bioinformatics tool (see Materials and Methods) that identified pathways enriched for the DE genes in each case. Among the top 20 pathways that were significantly involved (adjusted P -value < 0.05) according to the GO Biological Process 2015 database, 10 were related to T-cell regulation and/or activation (Fig 3D). Interestingly, important transcripts concerning T-cell activation (*IL2RA-CD25*) and T regulatory cell (Treg) differentiation (*FoxP3*) were found to be increased in MitoT^{pos} CD3⁺ T cells, while conversely, negative regulators of Treg differentiation such as *RORC* were decreased compared with MitoT^{neg} cells (Fig 3E). Finally, expression levels for selected DE genes involved in T-cell activation and Treg differentiation were additionally validated by qRT-PCR, corroborating the significant ($P < 0.05$) upregulation of *FoxP3*, *CTLA4*, and *GITR* mRNA levels (Fig 3F) seen in the RNA-Seq analyses of MitoT^{pos} compared with MitoT^{neg} cells (Fig 3G).

The sole transfer of mitochondria induces Treg cell differentiation

To assess whether MSC-MitoT impacts T-cell differentiation, functional analyses were performed using FACS-sorted T CD4⁺ naïve cells. Human PBMCs were mitocepted, stained, and sorted for naïve (CD4⁺CD45RA⁺CD45RO⁻) MitoT^{pos} and naïve MitoT^{neg} cell populations (Fig EV4E). These were then tested for *in vitro* differentiation in the absence or presence of Treg-inducing media (anti-CD3, IL-2, and TGF- β 1). Interestingly, in the absence of cytokine-based induction media cell clusters identified by bright-field microscopy evidenced a particular activation/proliferation status among MitoT^{pos} cells (Fig 4A). Furthermore, FACS analysis confirmed that marked levels of Treg differentiation occurred in MitoT^{pos} cells compared with the MitoT^{neg} condition (24% and $< 1\%$, respectively), revealing that MitoT alone was capable of driving Treg cell (CD25⁺FoxP3⁺) differentiation (Fig 4B). The percentage of Treg cells among MitoT^{pos} compared with MitoT^{neg} cells was significantly increased in both cultures,

Figure 3. Bioinformatic analysis of MitoT cells identifies changes in mRNA expression associated with T cell activation and differentiation pathways.

- Differentially expressed (DE) genes from whole transcriptome RNA sequencing analysis in FACS-sorted CD3⁺ MitoT^{neg} and CD3⁺ MitoT^{pos} cells from healthy human peripheral blood samples ($n = 4$ biological replicates, with 4 different donors of PBMCs).
- Volcano plot analysis derived from FPKM values showing DE genes ($P < 0.05$, Student's t test) in sorted MitoT^{neg} and MitoT^{pos} CD3⁺ cells (from four different donors of PBMCs).
- Heatmap depiction of RNA-Seq analysis of significantly ($P < 0.01$, Student's t test) DE coding genes from sorted MitoT^{pos} and MitoT^{neg} CD3⁺ cells (from four different donors of PBMCs).
- Significantly enriched pathways related to T cell regulation and activation for DE genes ($P < 0.05$, Student's t test) between MitoT^{pos} and MitoT^{neg} CD3⁺ cells, from the GO Biological Process 2015 database (from 4 different donors of PBMCs).
- Differentially expressed genes from the significantly enriched pathways listed in Fig 2D. Highlighted in red are key markers of Treg phenotype.
- qRT-PCR analysis of genes related to T cell activation after Mitoception with UC-MSC-MT ($n = 4$ biological replicates, with four different donors of PBMCs). The graph depicts fold expression in CD3⁺ MitoT^{pos} cells relative to CD3⁺ MitoT^{neg} cells, which are set at 1. Graph shows mean \pm SEM and statistical analysis by Student's t -test ($*P < 0.05$).
- Correlation analysis of 14 sampled genes between qRT-PCR and RNA-Seq, from MitoT^{pos} and MitoT^{neg} CD3⁺ cells (from 4 different donors of PBMCs). Graph depicts best-fit line and 95% confidence intervals by Pearson correlation analysis.

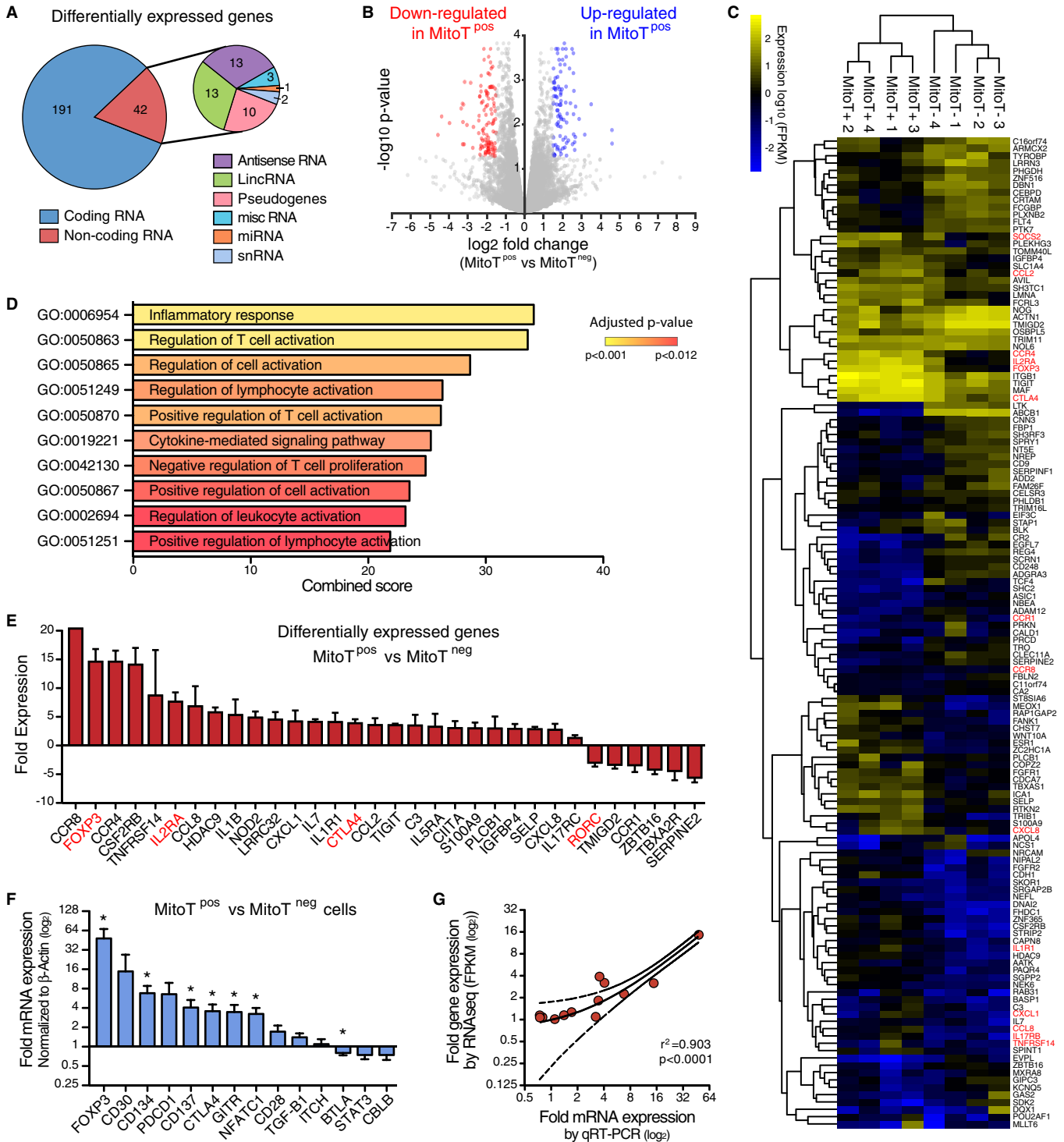


Figure 3.

with or without the differentiation media (19.8 versus 0.56; and 41.45 and 5.19, $P = 0.013$ and $P < 0.0001$, respectively; Fig 4C). Interestingly, MT from other sources including fibroblasts or PBMCs failed to obtain high frequency of Treg cells (4.4 and 1.4%, respectively; Fig EV4F), proving that the observed MitoT effect is source-dependent.

Further analysis on FACS-sorted T CD4⁺ naïve MitoT^{neg} compared with MitoT^{pos} cells differentiated into Treg cells showed a significant increase in the CD25⁺ICOS⁺ subset (average of 4.3 and 21.6%, respectively, $P = 0.0053$) and a decrease in the CCR7⁺ subset (average of 90.3 and 64.9%, respectively, $P = 0.0008$; Fig 4D and E), suggesting that MitoT^{pos} cells

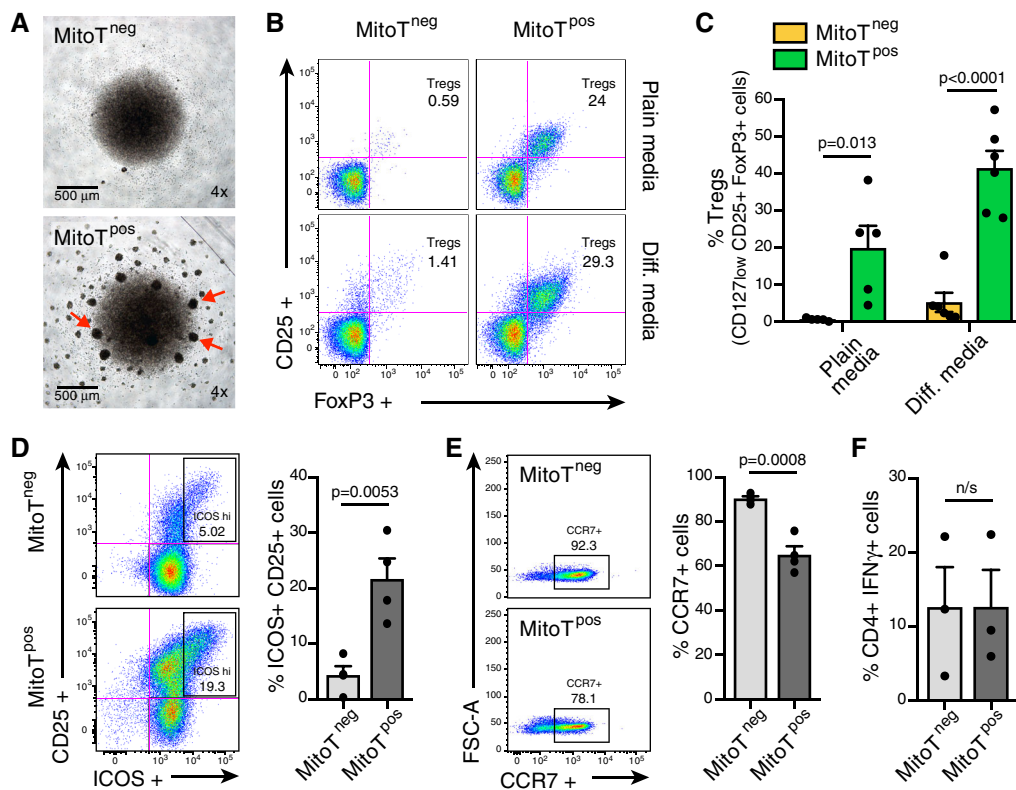


Figure 4. Efficient MitoT to T cells underlies functional changes including enhanced immunosuppression through regulatory T cell (Treg) induction.

A Representative bright-field microscopy images of FACS-sorted CD4⁺ naïve MitoT^{neg} (upper panel) and MitoT^{pos} (lower panel) cells after 5 days in culture with plain media (no cytokines added). Red arrows are indicative of activation/proliferation clusters.

B Representative FACS plots of Treg (CD127^{low}CD25⁺ FoxP3⁺) populations after T cell differentiation on media with or without cytokines and antibody supplements (anti-CD3, IL-2 and TGF-β1).

C FACS analysis of Treg induction after 5–7 days differentiation of FACS-sorted CD4⁺ naïve MitoT^{neg} and MitoT^{pos} cells in plain ($n = 5$) or differentiation media ($n = 6$) (Biological replicates, with different donors of PBMCs).

D ICOS expression on FACS-sorted CD4⁺ naïve MitoT^{neg} and MitoT^{pos} cells after 5–7 days in culture with differentiation media. Representative FACS plot (left panel) and bar graph (right panel) of ICOS high population ($n = 4$ biological replicates).

E CCR7 expression on sorted CD4⁺ naïve MitoT^{neg} and MitoT^{pos} cells after 5–7 days in culture with differentiation media. Representative FACS plot (left panel) and bar graph (right panel) of CCR7⁺ population ($n = 4$ biological replicates).

F FACS analysis of Th1 (CD4⁺ IFN-γ⁺) induction after 5–7 days differentiation of FACS-sorted CD4⁺ naïve MitoT^{neg} and MitoT^{pos} cells in plain media ($n = 3$ biological replicates). n/s = not significant.

Data information: In (C–F) graphs show mean ± SEM and statistical analysis by Student's *t*-test.

feature phenotypic characteristics of highly activated Treg cells [9,10]. Interestingly, no changes were observed on pro-inflammatory T-helper 1 (Th1; CD4⁺IFN-γ⁺) cells when comparing MitoT^{pos} and MitoT^{neg} cells cultured in plain media (Fig 4F). T-helper 17 (Th17; CD4⁺IL17⁺) cells were not detected under this condition.

MitoT-induced Treg suppress effector T cells

Next, we evaluated whether the phenotypic Treg cells obtained following MSC-MT induction retain their suppressive function. Using a co-culture assay with PBMCs from a different donor, previously stained with Cell Trace Violet (CTV), the capacity of the new Treg cells to inhibit proliferation (immunosuppression assay) was tested (Fig 5A). After 5 days in co-culture under PHA activation, FACS analysis showed that both MitoT^{neg} and MitoT^{pos}

Treg-induced cells inhibited the proliferation of target PBMCs. However, MitoT^{pos} Treg-mediated immunosuppression of PBMCs was significantly higher compared with MitoT^{neg} Treg cells, at both 1:1 (4.7-fold change) and 2:1 (fivefold change) cell ratios ($P = 0.0074$ and 0.0028 , respectively; Fig 5B and C, and EV4G).

MitoT significantly increased the survival rate of GVHD mice reducing the degree of tissue inflammation

Since CD4⁺CD25⁺Foxp3⁺ Treg cells are critical in the control of tolerance and autoimmunity and also implicated in human diseases including GVHD [11], we used this model to assess the functional impact of MitoT *in vivo*. To this end, we assessed the effect of mitocepted PBMCs in contrast with non-treated PBMCs in the induction of a murine model of GVHD. To gauge the expansion of the donor-derived and disease-inducing cells in the host, we employed a

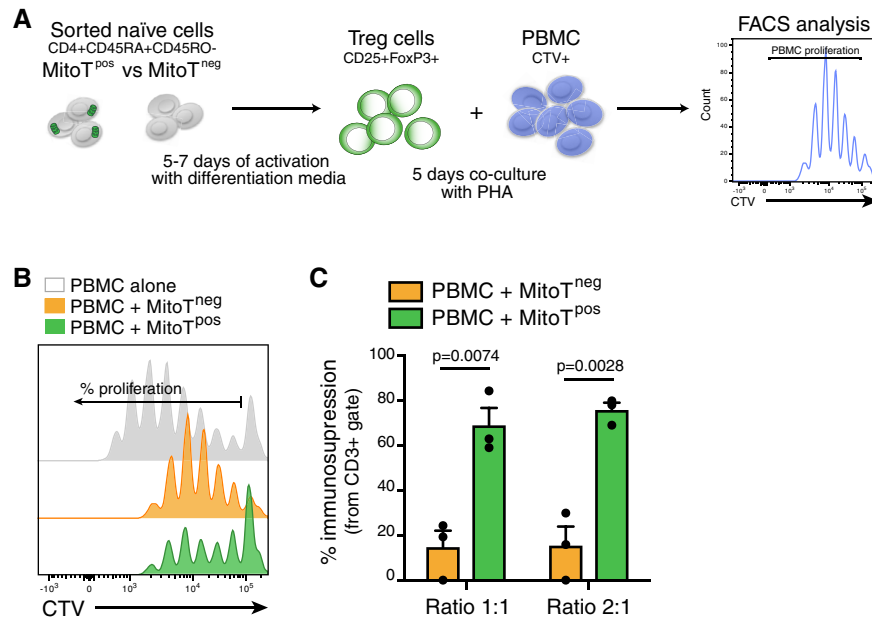


Figure 5. MitoT-induced Treg cells inhibit the proliferation of target PBMCs.

- A Schematic representation of the experimental design used for the immunosuppression assay.
- B Representative proliferation FACS histogram of CTV-stained PBMC co-cultured with MitoT^{neg} or MitoT^{pos} cells (ratio 1:1) after 5–7 days of CD4⁺ naive cell activation with Treg induction/differentiation media (anti-CD3, IL-2 and TGF- β 1). PBMC alone represents positive control of proliferation and PBMC co-culture with MitoT^{neg} correspond to the inhibition control with induced Treg cells.
- C Percentage of immunosuppression of CTV-stained PBMC co-cultured with MitoT^{neg} or MitoT^{pos} cells after 5–7 days of CD4⁺ naive cell activation with differentiation media (ratio MitoT cells:PBMC) ($n = 3$ biological replicates, with different donors of PBMCs). Graph shows mean \pm SEM and statistical analysis by Student's t -test.

human xenogeneic mouse model of GVHD (Fig 6A and B). Starting at 13 days post-GVHD induction, a significant difference in weight loss ($P < 0.05$) was observed comparing the PBMC-MitoT (88.5%) and control PBMC group (84.4%; Fig 6C). Moreover, the mitocepted PBMC-induced group displayed a significant improvement in mice survival rate compared with controls, with a median survival of 19 and 15 days, respectively ($P = 0.0218$; Fig 6D). Next, we evaluated the *in vivo* expansion and tissue infiltration of pro-inflammatory and anti-inflammatory human donor T cells in spleen, small intestine (SI), liver, and lung. After 8–9 days of GVHD induction, FACS analysis of splenocytes showed that CD4⁺CD25⁺Foxp3⁺ T cells were increased in the mitocepted group, yet not significantly (Figs 6E and EV5A and B), while the IFN- γ ⁺ pro-inflammatory cells showed a significant reduction in Th1 (CD4⁺IFN- γ ⁺; average of 23.6% for PBMC and 15.4% for PBMC-MitoT) and cytotoxic T CD8⁺IFN- γ ⁺ (1.2-fold change) populations ($P = 0.0011$ and $P = 0.0032$, respectively; Figs 6F and EV5C and D). No change was observed in Th17 cells (CD4⁺IL-17⁺ populations; Fig EV5E). Histopathological analysis showed that mice receiving mitocepted PBMCs had less pathological damage scores in the liver and SI compared with mice receiving control PBMCs (Fig 6G), with 34.7% ($P = 0.007$) and 25.35% ($P = 0.0395$) reduction in pathology scores for liver and SI, respectively (Fig 6H and I). Interestingly, we found that the number of Paneth (gut-regenerating) cells per crypt was significantly higher (1.6-fold) in mice receiving PBMC-MitoT compared with untreated PBMC-inducing protocol ($P < 0.0001$; Fig 6J). In lung tissues, histological analysis showed that mice receiving control PBMC displayed a dense mononuclear cell infiltrate surrounding both pulmonary

vessels and bronchioles and a severe pneumonitis involving both the interstitium and alveolar spaces (Fig 6K), while mitocepted PBMC-treated mice showed a 2.5-fold reduction in damage scores ($P < 0.0001$) compared with PBMC control group (Fig 6L). FACS analysis revealed a significant decrease in total human T CD4⁺ cells in lung tissues of PBMC-MitoT group versus PBMC control group ($P = 0.0059$; Fig 6M). These results suggest that the increased survival rate of mitocepted-PBMC mice is associated with a marked reduction in tissue injury of the main target organs affected in GVHD.

Systemic lupus erythematosus (SLE) is an autoimmune disease with inflammatory disorder of the connective tissues. The SLE model was selected to demonstrate the MitoT efficiency on inflammatory T cell *ex vivo*. Immune cells isolated from the spleen and lymph nodes from SLE mice (MRL/MpJ/Fas) showed a significant increased (10-fold) MitoT from UC-MSCs compared with control healthy mice (MRL/MpJ; Fig EV5F and G).

Discussion

Mitochondria as key players of cellular metabolism are critically important to understand T-cell function changes. MT status not only fuels active lymphocytes but as our data indicate also provides guidance for proliferation, migration, and cell fate decisions. Hence, MitoT might represent an amenable system to study functional changes in T cells while enabling improved cell-based treatments, since MSCs are a main cell source for MitoT [12]. The scope of such

immunometabolic and regulatory change has been in part addressed by Chen *et al* [13] who evidenced that UC-MSCs tended to correct the mitochondrial respiratory dysfunction and increased T-cell apoptosis of SLE patients, in concomitance with MitoT to PBMCs *in vitro*. While most of the work regarding mitochondrial delivery from one cell to another involves the rescue of damaged cells by healthy ones, no study to date has shown the physiological or artificial transfer to healthy lymphocytes. In this work, we assemble direct evidence for

a reproducible, rapid, dose-dependent, and efficient MitoT from cultured MSCs to T and B lymphocytes isolated from healthy donors. Since MitoTracker-labeled MT can leak dye over time, control experiments were necessary to confirm the real uptake of MT. The suppression of MitoT at 4°C and the detection of only human-specific mitochondrial genes (qPCR) but no human β -microglobulin genes in murine UC-MSC-co-cultured murine lymphoid cells confirmed the mediation of an energy-dependent

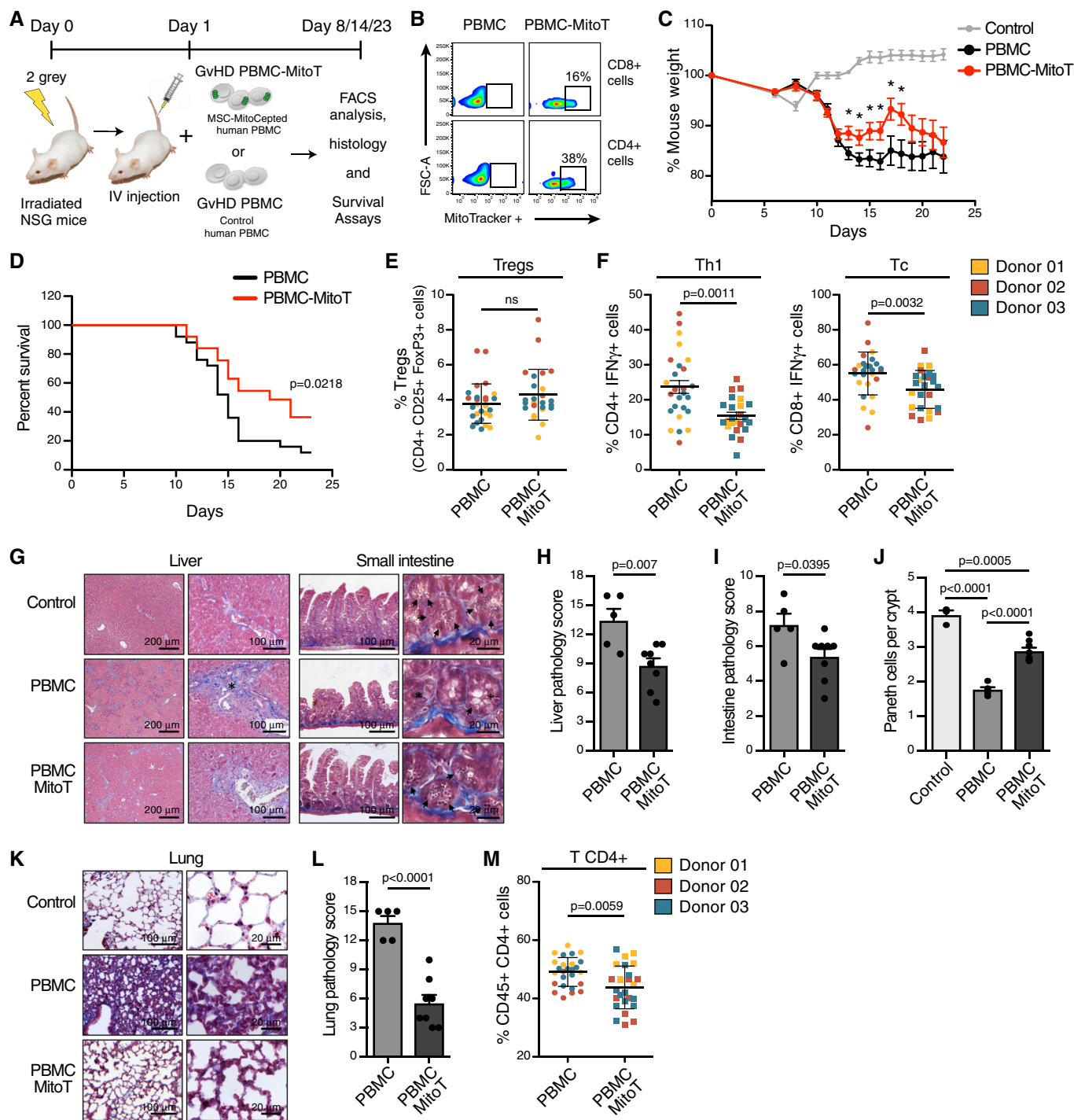


Figure 6.

Figure 6. Xeno-GVHD induction with MitoT^{POS}-PBMCs is associated with improved survival and reduced tissue inflammation in a mouse model of disease.

- A *In vivo* experimental design of human xenogenic model of GVHD in NSG immunodeficient mice, with MSC-mitocepted human PBMC transplant.
- B Representative FACS plots of Mitoception (% of MitoTracker+) in CD4⁺ or CD8⁺ T cells from mitocepted PBMC compared to control PBMC, before intravenous injection.
- C Percent of mouse weight after GVHD induction with IV injection of mitocepted PBMC or control PBMC cells ($n = 3$, with a total of 25 mice per group). Control group in grey, were untreated mice ($n = 6$ mice). * $P < 0.05$ by Mann Whitney *t*-test.
- D Kaplan Meier plot showing percent survival of GVHD mice after transplantation of an equal amount (1.2×10^6 cells) of mitocepted PBMC or control PBMC cells ($n = 3$, with a total of 25 mice per group) ($P = 0.0218$ by log-rank test).
- E FACS analysis of human Treg (CD4⁺ CD25⁺ FoxP3⁺) cell engraftment in mouse spleen following transplantation of PBMC-MitoT or control PBMC cells ($n = 3$, with a total of 25 and 27 mice per group, respectively).
- F FACS analysis of human pro-inflammatory T helper1 (CD4⁺ IFN- γ ⁺, left panel) and T cytotoxic (CD8⁺ IFN- γ ⁺, right panel) cell engraftment in mouse spleen following transplantation of mitocepted or control PBMC cells ($n = 3$, with a total of 25 and 27 mice per group, respectively).
- G Representative histopathologic images of GVHD in liver and small intestine sections obtained from PBMC-MitoT, PBMC and non-transplanted control samples, stained with Masson's trichrome staining. Asterisk showed increased periportal collagen deposits in the liver and increased piknotic cells in the small intestine crypts. Arrowheads represents a reduced number of Paneth cells.
- H, I Semiquantitative scoring system for pathologic damage in the liver and small intestine of mitocepted PBMC ($n = 8$ independent mice) or control PBMC transplanted mice ($n = 5$ independent mice).
- J Quantification of Paneth cells per crypt, from at least 50 crypts per PBMC-MitoT ($n = 8$ mice), PBMC transplanted ($n = 5$ mice) or non-transplanted control ($n = 3$) mouse.
- K Representative histopathologic images of GVHD in lung sections obtained from PBMC-MitoT, PBMC and non-transplanted control, stained with Masson's trichrome staining.
- L Semiquantitative scoring system for pathologic damage in lung of mitocepted PBMC ($n = 8$ independent mice) or control PBMC transplanted mice ($n = 5$ independent mice).
- M FACS analysis of total human CD4⁺ cell engraftment in mouse lungs following transplantation of mitocepted PBMC or control PBMC cells ($n = 3$, with a total of 25 and 27 mice per group, respectively).
- Data information: (E–M) represent mice from three independent *in vivo* experiments. In (E–F, H–J and L–M), graphs show mean \pm SEM and statistical analysis by Student's *t*-test.

process, not attributable to cell fusion nor dye-related artifact. MT trafficking was found to be independent of pre-conditioning, pro-inflammatory, or anti-oxidant treatment of MSCs or mitogen stimulation of target PBMCs.

Mesenchymal stem cells are known to establish tunneling nano-tube connections (TNTs) with target cells, including cardiomyocytes, endothelial cells, and tumor cells [12]. Also, TNT formation was described between MSCs and macrophages leading to an enhanced phagocytosis activity [6]. For this reason, we tested the effect of cytochalasin D, an inhibitor of TNT formation in the co-culture condition, finding no interference of the inhibitor on the levels of MitoT. Mindful of other possible mechanisms sustaining MitoT, including gap junctions, hemi-channels, and macropinocytosis, and corresponding inhibitors such as lanthanum III chloride hydrate, carbenoxolone, and EIPA ((5'*N*-ethyl-*N*-isopropyl) amiloride) were used, with MitoT remaining unaffected. Phinney *et al* [14] described the use of extracellular vesicles (EVs) by MSCs to shuttle MT, that were subsequently engulfed by macrophages, resulting in increased macrophage bioenergetics. In consideration of this finding, PBMCs were incubated with conditioned media from MitoTracker-labeled MSCs; nonetheless, no MitoT was detected. Probably, certain signals from recipient cells that trigger this phenomenon remain necessary. In this regard, a recent study described MT transfer mediated by the adhesion molecule ICAM-1 between Jurkat cells and MSCs, where treatment with a neutralizing antibody against ICAM-1 led to partial inhibition of MitoT [15]. In contrast with our results, Wang *et al* [15] showed that while both ALL T cells and Jurkat cells can transfer MT to MSCs, they receive almost no MT from MSCs, resulting in chemoresistance. Within our experimental setting, we also observed a unidirectional transfer; however, contrarily to the above study, MitoT was uniquely observed from MSCs to PBMCs. This divergence in the direction of the transfer can be due to the tumoral nature of the cells used in the

Wang *et al* study in comparison with the primary cells we used from healthy individuals. Future research should explore the existence of a two-way transfer of MT among MSCs and PBMCs, from donors of different disease conditions, and how these parameters affect MitoT efficiency. *In vivo*, we could also evidence the natural transfer of MT in response to intraperitoneal infusion of MSCs in immune-competent mice. To overcome the limitation of dye fading in this case, the use of cells with a stable MT reporter [16] will allow improved monitoring of this phenomenon, including more precise quantitation of biodistribution and fate at longer time points.

Since active and functional MT are able to maintain an electrochemical gradient, known as the MMP, we demonstrated the functionality of our isolated MT from UC-MSCs using MitoTracker Red CMXRos and TMRM, both dyes accumulate in active MT with an intact MMP, as well as measurement of ATP production, as previously reported by other groups [7,17–19]. We then assayed functional changes resulting from the MitoT to CD3⁺ T cells including the effect on proliferation, metabolism, migration, and differentiation. While no direct effect was observed on proliferation, preliminary metabolic analysis of MitoT^{POS} PBMCs revealed a decrease in maximum respiration compared with MitoT^{NEG} cells. Regarding lymphocytes, it has been shown that effector T cells have a substantially lower maximal respiration than memory T cells [2,20], suggesting that T cells may enter in an activated state when mitocepted. Additionally, MitoT^{POS} cells displayed a 50% increase in the glycolytic/OXPHOS ratio, which is a hallmark of T-cell activation [21,22]. Activated MitoT^{POS} CD3⁺ cells also showed significant increases in migration capacity compared with MitoT^{NEG} cells. MT localization and fission have been reported to positively affect migration, suggesting a role in breast cancer metastasis [23]. MT are also implicated in lymphocyte adhesion, polarity, and migration, in correlation with the expression of Miro-1, an adaptor molecule that couples MT to microtubules [24].

To further encompass a wider range of functional changes related to MitoT, transcriptome analysis was performed on sorted T CD3⁺ populations, according to MT uptake. Bioinformatic analysis on the two distinct populations (MitoT^{pos} and MitoT^{neg}) showed that the most significant changes in mRNA expression levels were found in Treg activation pathways, including FOXP3, IL2RA, CTLA4, and TGF- β 1. Indeed, naïve MitoT^{pos}-sorted T cells were driven toward a CD127^{low}CD25⁺FoxP3⁺ (Treg) suppressor phenotype as opposed to MitoT^{neg} cells (fold change of 14). Thus, the displayed evidence points to the independent capability of MitoT to curb pro-inflammatory T cells while directing cell fate toward a Treg phenotype *in vitro*, even in the absence of the exogenous cytokine stimulation usually required for such T-cell differentiation. In 2013, our group had demonstrated that MSCs are able to generate a CD4⁺CD25⁺Foxp3⁺ Treg population, even during the differentiation process of Th1 and Th17 cells [25]. Many mechanisms behind this observation have been forwarded since, including ubiquitination [26], jagged-1-dependent pathway [27], and miRNA modulation [28] resulting in the induction of stable expression of Foxp3. Herein, we unexpectedly identified a novel mechanism of Treg induction by MSCs based on MitoT alone.

While MT are critically involved in the regulation of T-cell activation, differentiation, and expansion, they are also involved in modulating signaling in T cells through different mechanisms including mitonuclear communication induced by the hormetic response (mitohormesis). The metabolism changes rely in a variety of signals among which are MT dynamics, mROS, and metabolite and mitokines production. These MT-derived metabolites may provide signals for the activation and differentiation toward a Treg fate. Indeed, one report has shown that S-2-hydroxyglutarate (S-2HG) acts as an immunometabolite, driving the T-cell differentiation through epigenetic changes that alter the gene expression profile [29]. Future metabolomic investigation is required to determine the effect of MitoT on immunometabolite changes that affect T-cell fate.

Additionally, MitoT might also induce a retrograde MT-to-nuclear signaling. This feedback transmits mitochondrial signals such as transcription factors leading to changes in nuclear gene expression and a reconfiguration of metabolism to accommodate cells to MT status changes. While much is still unknown about such signaling pathways in mammalian cells; recently, sirtuin (SIRT) and G-protein pathway suppressor 2 (GPS2) were identified as a molecular mediator of mitochondrial retrograde communication. Their transcriptional activity is in fact directly regulated by the MT functional status through regulated MT-to-nucleus translocation [30]. Furthermore, GPS2 activity has recently been reported to play a role in B-cell development also [31]. Future directions related to this work will consider evaluating the effect of GPS2 in the context of MitoT while establishing the possible correlation with the activation of the FOXP3 pathway.

In addition to our transcriptomic data, cell phenotyping also sheds some light on the resultant cell type, since we found increased CD25⁺ICOS⁺ cells, with decreased CCR7 expression.

A CD4⁺CD25⁺ Treg subpopulation characterized by an ICOS⁺FoxP3⁺ phenotype has been identified among Treg cells [32,33] featuring a highly and more efficient suppressive capacity compared with its ICOS^{neg} counterpart [10,34]. ICOS⁺ Treg cells have been directly related to a higher expression of cytotoxic T-lymphocyte-associated protein 4 (CTLA-4), essential in Treg generation [35,36], and

stabilization of the expression of FoxP3 [10,37]. CCR7 is described as a potent chemotactic receptor [38], under inflammatory conditions, and the activation of quiescent Treg cells results in the loss of CCR7 marker, allowing newly activated Treg cells to redistribute to inflamed sites [9,39,40]. Interestingly, the maintenance of CCR7 low-activated Treg cells in non-lymphoid organs depended on the ICOS pathway [9] that we also found upregulated in response to MitoT.

The action of CD4⁺CD25⁺Foxp3⁺ Tregs is pivotal in the prevention and treatment of acute GVHD, both in animal models [41] and in clinical settings [42]. The expression of inhibitory CTLA-4 molecules, lymphocyte-activation gene 3 (*LAG-3*), and neuropilin-1 contribute to the inhibition of co-stimulatory markers resulting in decreased proliferation of T cells [43]. This is convergent with the results in our *in vivo* xeno-GVHD disease model in response to MitoT^{pos} cell disease induction as compared to non-treated cells, showing significant improvements in survival and weight loss, and reduction in tissue damage (lung, liver, and gut) and organ infiltrating CD4⁺, CD8⁺ ($P < 0.05$), and IFN- γ ⁺ cells ($P < 0.0001$). These results substantiate that MitoT of MSCs into T cells is able to modulate the pro-inflammatory signature of T cells, inducing functional Treg cells *in vivo* and prompting a diminished pro-inflammatory state that leads to beneficial clinical effect. This was associated with significantly higher number of Paneth cells per crypt (1.6-fold) in mice receiving PBMC-MitoT, also in line with the fact that the number of Paneth cells located in the base of intestinal crypts has been inversely correlated with the outcome and severity of clinical GVHD [44,45]. Thus, the increased survival rate of GVHD animals induced by mitocepted PBMCs is convergent with the *in vitro* effects of MitoT, the transcriptomic profile of target cells, and the phenotypic profile of the resultant Treg cell.

In summary, this study reports for the first time the natural and artificial horizontal transfer of MSC-derived MT to human T-cell populations. We also provide evidence that MitoT alone was self-sufficient for inducing Treg cell differentiation with no need for the release of other paracrine factors or exosomes, when target cells were subjected to a Mitoception protocol. Furthermore, mitocepted disease-inducing cells regulated the inflammatory response and tissue damage leading to improved survival in a GVHD pre-clinical model. These findings point at a new mechanism for MSC-mediated control of immune-mediated diseases based on MitoT from MSCs to immunocompetent cells. In conclusion, we demonstrated that mitocepted T cells undergo distinct metabolic reprogramming and propose that promoting Treg induction may represent a promising strategy to control inflammatory immune-mediated diseases epitomized by GVHD. While shedding light on this new immunoregulatory mechanism, our findings offer strategies to improve cell-based therapies or eventual cell-free therapeutic approaches.

Materials and Methods

Cell isolation and culture

Peripheral blood samples were collected from healthy donors, previously informed consent, and Ficoll-Paque PLUS density gradient media was used for the isolation of mononuclear cells (PBMCs). UC-MSC, bone marrow (BM), and menstrual (Mens)-derived MSCs were cultured, expanded, and fully characterized according to

international guidelines, as previously described [46,47] (Table EV1). All the experiments were performed using MSCs at early passages (P3–P7) and fresh PBMC cultured with 10% FBS, 1% Pen/Strep, 1% sodium pyruvate, 1% non-essential amino acids, 1% glutamine, and 25 μ M β -mercaptoethanol in RPMI media (lymphocyte media). When indicated, UC-MSCs were pre-activated for 24 h with 20 ng/ml of IFN- γ and 10 ng/ml of IL-1 β , as previously described [48,49] or incubated over night with increasing concentrations of the anti-oxidant pterostilbene (Ptsb). All the procedures presented in this work were approved by the Ethics Committee of Universidad de los Andes.

Co-culture assay and flow cytometry analysis

Umbilical cord-MSCs were labeled the day before the experiments with MitoTracker Green FM, MitoTracker Red CMXRos, or MitoTracker Deep Red FM (Molecular Probes, Eugene, OR, USA), according to manufacturer's instruction, and plated using 48-well plates. For co-culture assays, different MSC:PBMC ratios were used, and after UC-MSC media was removed, 5×10^5 freshly isolated PBMCs were plated on top of the MSCs with the lymphocyte media as mentioned above. After 24 h, cells were collected, washed with PBS, and, when indicated, stained at 4°C for 20 min using specific antibodies for human CD45-PECy7 (#557748, 1:100), CD3-APC (#555335, 3:100), CD19-V450 (#644491, 1:200), and CD56-APC (#555518, 3:100) from BD Biosciences (Franklin Lakes, NJ, USA); and CD4-PECy7 (#317414, 1:500) and CD8-PECy5.5 (#301032, 3:100) from BioLegend (San Diego, CA, USA). In control experiments, MSCs were also stained with either anti-CD90-PECy7 antibody (#561558, 1:50 from BD Biosciences) or CTV dye (Thermo Fisher Scientific, Waltham, MA, USA), according to manufacturer's instruction. For T-cell differentiation assays, cells were stained with specific surface antibodies against human CD127-V450 (#560823, 1:100, BD Biosciences), CD25-PerCP-Cy5.5 (#560503, 1:50, BD Biosciences), CD278 (ICOS)-APC (#313509, 1:500, BioLegend), and CD197 (CCR7)-Pacific blue (#353209, 1:100, BioLegend). For intracellular staining, cells were fixed at 4°C with the forkhead box P3 (FoxP3) staining buffer set (eBioscience Inc, San Diego, CA, USA) and then incubated for 30 min with anti-FoxP3-PE (#12477442, 1:100), anti-IFN- γ -APC-eFluor 780 (1:100; eBioscience), or anti-IL-17-PerCP-Cy5.5 (#560799, 1:100, BD Biosciences). For humanized xenogenic-GVHD mouse model experiments, cells were stained with CD45-PerCP (#347464, 1:100), CD8-PE (#555367, 1:100), CD25-PerCP-Cy5.5 (#560503, 1:100), and IFN- γ Alexa Fluor 488 (#557718, 1:100) from BD Biosciences, and CD4-PECy7 (#317414, 1:300, BioLegend) and FoxP3-FITC (#11477741, 1:100) from eBioscience. After staining, cells were washed and labeled with the near-IR or yellow fluorescent reactive dye for cell viability (Live/Dead Fixable Near-IR or Yellow Dead Stain Kit, from Thermo Fisher Scientific). Data were acquired using FACS Canto II and analyzed with the FlowJo software.

Microscopy

Confocal microscopy of live PBMCs after co-culture with MSCs was done with a Carl Zeiss LSM 700 confocal laser system. MSC-MT were labeled with MitoTracker Green, and PBMCs were stained with a lymphoid-specific antibody for human CD3-Alexa Fluor 647

(#300422, 1:25 from BioLegend). Confocal microscopy of fixed co-cultures or mitocepted PBMCs was performed with a Leica TCS SP8 confocal laser system using MitoTracker Green for staining MSC-MT and MitoTracker Red CMXRos to label endogenous PBMC MT. Cells were seeded on a cover slide previously coated with poly-lysine (Sigma-Aldrich, St. Louis, MO, USA). After 3 h of co-culture or 24 h post-mitoception, cells were fixed in 10% formalin solution (Sigma-Aldrich), stained with DAPI or Hoechst (nuclear staining), and mounted with Dako fluorescent mounting medium (Dako North America Inc., CA, USA).

Transmission electron microscope images were taken with a Philips Tecnai 12 Biotwin TEM Electron Microscope. Mitoception was performed on freshly isolated PBMCs, and FACS-sorted CD3⁺ MitoT^{neg} and MitoT^{pos} T cells were fixed with fresh glutaraldehyde solution. Samples were then processed at the Advanced Microscopy Unit at the Pontificia Universidad Católica de Chile.

DNA and RNA extraction, and quantitative RT-PCR

Total DNA was isolated from human UC-MSC, mouse spleen cells from MRL/MpJ mice (The Jackson Laboratory, Bar Harbor, ME, USA), or FACS-sorted CD45⁺ previously co-cultured mouse spleen cells, using QIAamp DNA Mini Kit (Qiagen, Hilden, Germany), following the manufacturer's instructions. qPCR was performed in duplicate on a Stratagene Mx3000P with the use of Brilliant II SYBR Green Master Mix (Agilent Technologies, Santa Clara, CA, USA). For whole-genome RNA-Seq analyses and qRT-PCR, total RNA was isolated from 500,000 FACS-sorted CD3⁺ MitoT^{pos} or CD3⁺ MitoT^{neg} cells, previously resuspended in RLT lysing buffer (Qiagen, Hilden, Germany), using RNeasy Micro Kit from Qiagen and following the manufacturer's recommendations. Complementary DNA was prepared in a reverse-transcription reaction using 200–250 ng of RNA and SuperScript II Reverse Transcriptase (Thermo Fisher Scientific). Five nanogram of template mRNA and 5 μ M of each forward and reverse human-specific primers (Table EV2) were used. Data were expressed as relative gene expression or fold mRNA expression using the $2^{-\Delta\Delta Ct}$ method and normalized to β -actin housekeeping gene.

In vivo mitochondrial transfer

MitoT from human MSCs to murine lymphoid cells was assessed using a BALB/c mouse model. Animals were kept at specific pathogen-free animal facility of Universidad de los Andes with water and food *ad libitum*, according to international guidelines for animal care and protocols approved by the Institutional Animal Care and Use Committee (ARRIVE Guidelines Animal Research) and approved by the local animal care committee (number CEC201729, June 30, 2017). Mice were firstly immunized using an intraperitoneal injection of CFA emulsion (100 μ l of CFA suspension diluted 1:1 in PBS 1 \times). At 24 h post-immunization, mice were intraperitoneally injected with 5×10^6 human UC-MSCs, previously stained with MitoTracker Green, as described above. Euthanasia was performed 24 h after cell injection, and mouse organs were collected and mechanically disrupted for cell extraction in PBS 1 \times supplemented with 2% FBS and 2 mM EDTA. Cells were stained using a specific antibody for human CD90-Pacific Blue (#561558, 1:100, BD Biosciences) and labeled with the live/dead near-IR fluorescent dye (as described above). Data were acquired using a FACS Canto II,

and total leukocyte population was analyzed with the FlowJo software.

Mitochondria isolation and artificial transfer (Mitoception)

Umbilical cord-MSC-MT were isolated using the MT Isolation Kit (Thermo Fisher Scientific) following manufacturer's instructions, from previously MitoTracker-labeled donor cells. MT preparations were done using a range of $1-10 \times 10^6$ MSCs resuspended in the lymphocyte media (as described above) and maintained on ice until the artificial transfer was done (around 2–3 h). Mitoception was performed on PBMCs as previously reported [7], using the amounts of MSC-MT corresponding to the same cell number ratios used in co-culture experiments (MSC:PBMC ratios of 1:100, 1:25, and 1:10). The following day, cells were washed with PBS and used for experimental procedures.

Confocal microscopy on isolated MT

Umbilical cord-MSCs were previously labeled with MitoTracker Red CMXRos (Invitrogen, M7512), according to manufacturer's instruction, and isolated MT were resuspended in lymphocyte media and mounted on a microscope glass slide to be immediately visualized by the confocal microscope Leica Sp8.

Flow cytometry on isolated MT

Isolated MSC-MT were resuspended in lymphocyte media and stained with 200 nM of tetramethylrhodamine (TMRM; Invitrogen, T668), for 30 min at 37°C. For positive control, isolated MT were previously treated with 0.2 μ M of CCCP (carbonyl cyanide 3-chlorophenylhydrazone; CCCP; C2759, Sigma-Aldrich) for 5 min at 37°C. MT were gated based on light-scattering properties in a SSC versus FSC plot, and at least 2,000 events were recorded for each sample using a BD FACS Canto II Flow Cytometer. Histograms showing PE fluorescence were analyzed, and the mean fluorescence intensity (MFI) of each sample was calculated using FlowJo software (version 10).

ATP determination of isolated MT

ATP production was measured using the CellTiter-Glo[®] Luminescent Cell Viability Assay (Promega, G7570), according to manufacturer's instruction. Isolated MSC-MT were resuspended in 50 μ l of lymphocyte media and plated in an opaque 96-well plate. In each sample, 50 μ l of CellTiter-Glo[®] Reagent was added and the plate was incubated for 30 min at room temperature, followed by a luminescence reading using a BioTek FLx800 microplate reader.

Western blot analysis

CD3⁺ MitoT^{pos} and CD3⁺ MitoT^{neg} T cells were FACS-sorted at 24, 48, and 72 h post-mitoception with MSC-MT and resuspended with 50 μ l of cold RIPA buffer containing protease/phosphatase inhibitors (Cell Signaling Technology, #5872). Samples were then sonicated for 5 min at high intensity and centrifuged at 16,100 g for 15 min at 4°C to discard cellular debris. Supernatants containing proteins were collected, and protein quantification was performed

using the Bradford method following the manufacturer's instructions (Bio-Rad, #500-006). Twenty to thirty microgram of total protein was loaded and run in 10% SDS-PAGE gels. Five percent of BSA in PBS-Tween (0.01%) was used for blocking and primary antibodies were used in a dilution of 1:1,000 prepared in PBS-Tween (0.01%), over night with agitation at 4°C (all antibodies were purchased from Cell Signaling Technology: α -OPA1 #67589, α -MFN1 #14739, α -MFN2 #9482, α -DRP1 #14647, α -phospho-DRP1 Ser616 #4494, and α - β -actin #3700). Secondary fluorescent antibodies were prepared in a dilution of 1:20,000 in 5% BSA in PBS-Tween (0.01%); secondary antibodies were purchased from Invitrogen: α -mouse Alexa Fluor 680 #A32729 and α -rabbit Alexa Fluor 800 #A32735). Finally, fluorescence was detected using Odyssey[®] CLx and image analysis was made using Image Studio Lite software (version 5.2).

Metabolic measurements by extracellular flux analysis

Live-cell metabolic measurements of OCR and ECAR were performed with the Seahorse XF24 Flux Analyzer instrument (Seahorse Bioscience, North Billerica, MA, USA), in order to test mitochondrial respiration and glycolysis, respectively. Mitoception was performed on freshly isolated PBMC, and FACS-sorted CD3⁺ MitoT^{neg} and MitoT^{pos} cells were plated on a 24-well plate (500,000–700,000 cells per well, samples run in quadruplicates) with XF buffer. OCR (pmol/min/cell) was measured for 2 h using the following mitochondrial inhibitors: oligomycin (10 μ M), FCCP (2.5 μ M), antimycin A (20 μ M), and rotenone (20 μ M). Basal respiration rate was calculated as the difference between basal OCR and OCR after rotenone and antimycin A addition, where maximum respiration rate was measured following inclusion of the uncoupler FCCP.

Extracellular acidification rate (mpH/min/cell) measurements were quantified using glucose (10 mM) and oligomycin (10 μ M). Basal glycolysis was calculated as the difference between basal ECAR and ECAR upon glucose addition. All Seahorse measures were normalized to the number of cells counted in each well seeded before Seahorse experiments.

Lactate detection assay

L(+)-Lactate concentrations were measured from supernatants of FACS-sorted CD3⁺ MitoT^{neg} and MitoT^{pos} T cells, previously mitocaptured with UC-MSC-MT, using a commercially available kit from BioVision, Inc. (Milpitas, CA, USA), and following the manufacturer's recommendations. MitoT^{neg} and MitoT^{pos} cells were cultured at 37°C for 24 h in lymphocyte phenol red-free media. Then, cells were counted, and supernatants were collected and kept at –80°C until fluorometric quantification of lactate was performed.

Transmigration assay

T-cell migration was evaluated using a 24-well plate with 3.0- μ m-pore size Transwell polycarbonate membrane insert (Costar, Kennebunk, ME, USA). Freshly isolated and mitocaptured human PBMCs were FACS-sorted into CD4⁺ MitoT^{pos} and MitoT^{neg} populations and cultured at 37°C for 3 days with activation media (lymphocyte media with anti-CD3 [3 μ g/ml] and IL-2 [50 U/ml]), or

control media (no cytokines added). Afterward, cells were collected and 150,000 cells in 100 μ l of lymphocyte media were seeded on the top chamber of the Transwell wells. The bottom chamber was filled with 600 μ l of lymphocyte media to allow transmigration. After 4 h of incubation at 37°C, T cells that had migrated into the bottom chamber were collected and counted under the microscope with trypan blue staining for cell viability.

Proliferation assay

Freshly isolated human PBMCs were mitocepted with UC-MS-C-MT, stained with CTV dye (as described above), and cultured at 37°C in the presence of 15 μ g/ml of phytohaemagglutinin (PHA). After 3–4 days, cells were collected and stained with CD3-APC (3:100) from BD Biosciences, and labeled with live/dead fixable near-IR. Similar proliferation rates were measured in FACS-sorted CD3⁺ MitoT^{neg} and MitoT^{pos} T cells following 3 h of co-culture with MitoTracker Green-labeled UC-MS-C. Both groups were stained with CTV dye and cultured at 37°C for 5 days with CD3/CD28 Dynabeads (1/20; Thermo Fisher Scientific), IL-2 (50 U/ml), and PHA (15 μ g/ml). Data were acquired using FACS Canto II and analyzed with the FlowJo software.

Transcriptome profiling, differential expression analyses, and GSEA

Whole-genome RNA-Seq was performed at the DNA Array Core Facility at Scripps Research Institute (CA, USA) using an Illumina NextSeq 500 instrument. Raw reads were trimmed with the clipping of the first 10 bases in each extremity using Trimmomatic version 0.36 [50] when their quality average falls below the quality threshold of $Q < 30$. A five-base sliding window quality filtering was also performed, eliminating reads when the average quality of a window falls below $Q < 30$. Reads shorter than 15 nt after trimming were discarded, and the resulted clean data were mapped to the human genome GRCh38 [51] using HISAT2 version 2.0.5 [52]. SAM files generated on the mapping process were used as input to the Cufflinks protocol described by Trapnell *et al* [53], in order to obtain DE genes, using the GTF annotation file recovered from Ensembl database for the human genome GRCh38 [51]. Transcripts were considered as statistically DE when presenting a fold change bigger to 1.5 and a P -value smaller than 0.05. Web-based Enrichr bioinformatics tool [54] was used to identify gene ontology terms for the DE genes. We used webCEMiTool (<https://www.ncbi.nlm.nih.gov/pmc/articles/PMC6414412/>) with standard parameters to identify co-expressed modules in the RNA-Seq data, and to perform GSEA, as well as the over-representation of identified gene modules. The sets of functional categories were provided by webCEMiTool and Molecular Signatures Database (MSigDB) [55].

T-cell differentiation assays

Freshly isolated human PBMCs were mitocepted with MT from different sources, including UC-MS-C, fibroblast, or PBMCs. Following Mitoception protocol was described above, and cells were collected and stained at 4°C for 30 min with antibodies against CD4-PECy7 (1:500; BioLegend), CD45RA-V450, and CD45RO-APC (1:200; both from BD Biosciences). Then, MitoT^{pos}

and MitoT^{neg} CD4⁺ naïve cells (CD45RA⁺CD45RO⁻ population) were FACS-sorted and cultured at 37°C for 5–7 days on Treg induction/differentiation media: lymphocyte media with human anti-CD3 (3 μ g/ml), IL-2 (50 U/ml), and TGF- β 1 (10 ng/ml) or cultured on plain media (lymphocyte media with no cytokines added). Afterward, cells were collected and analyzed for Treg or for effector Th1 and Th17 lymphocyte differentiation by FACS analysis described above.

Immunosuppression assay

FACS-sorted CD4⁺ naïve MitoT^{neg} and MitoT^{pos} cells previously cultured in Treg induction/differentiation media (as mentioned above for T-cell differentiation assays) were co-cultured, for 5–7 days at 37°C with freshly isolated and CTV-stained PBMCs from a new donor (described above), in lymphocyte media supplemented with PHA (15 μ g/ml). Two different ratios of MitoT cells:PBMC were tested (1:1 and 2:1). Following co-culture, cells were collected and stained for FACS analysis, as described above. Proliferation rate and percentage of immunosuppression were analyzed with FlowJo software, looking at CTV⁺CD3⁺ populations. For immunosuppression analysis, the division index was calculated for each condition and values were obtained following the equation: $1 - (\text{Div. Index} / \text{Div. Index control}) * 100$.

Humanized xenogenic-GVHD mouse model

NOD-scid IL2rcnull (NSG) mice from The Jackson Laboratory (Bar Harbor, ME, USA) were kept at specific pathogen-free animal facility of Universidad de los Andes with water and food *ad libitum*, according to international guidelines for animal care and protocols approved by the Institutional Animal Care and Use Committee (ARRIVE Guidelines Animal Research) and approved by the local animal care committee (number CEC201729, June 30, 2017). Ten- to twelve-week-old mice were irradiated using a dose of 2 Gy at the Chilean Commission for Nuclear Energy Facilities. At 24 h post-irradiation, animals were randomized and injected through the tail vein with 12×10^6 mitocepted or control (same donor) human PBMCs obtained from buffy coats of healthy donors as described above. The onset of the GVHD progression occurs typically 7 days post-PBMC injection. Euthanasia of mice was performed at day 8–9 for immunological analysis by FACS, and at day 14 for histological analysis, or when a total body weight loss was $> 20\%$ of original starting weight. Target organs including spleen, liver, and lung were harvested from each group for specific human immunophenotypic, no blinding, analysis (see flow cytometry analysis section), in order to detect the presence of human pro-inflammatory and anti-inflammatory lymphocytes within the mouse tissue samples by FACS.

Histopathological analysis

Liver, SI, and lung samples from GVHD mice were harvested 14 days after PBMC injection, fixed in 4% paraformaldehyde, and embedded in paraffin. Five- μ m-thick sections were processed for hematoxylin–eosin and Masson's trichrome staining for detailed histological examination. Coded slides were examined systematically, in a blinded fashion, using a semi-quantitative scoring system for pathological alterations known to be associated with GVHD

[56–60]. The severity of histopathological changes in the lung was scored using two parameters: periluminal inflammatory cell infiltrates (around airways/vessels) and pneumonitis (alveolar/interstitial), following the system described by Cooke *et al* [56]. Briefly, the pathology score for each parameter was generated by multiplying the severity grade (0–3) by the extent of involvement (5–25% = 1; > 25–50% = 2; > 50% = 3; range of 0–9 in each parameter). A total lung pathology score was finally calculated by adding the pathology scores for pneumonitis and periluminal infiltrate (range of 0–18). On the other hand, seven parameters were scored for SI (villous blunting, crypt regeneration, loss of enterocyte brush border (ulceration), luminal sloughing of cellular debris, pyknotic crypt cells, outright crypt destruction, and lamina propria inflammatory cell infiltrate) and 11 parameters for liver (portal tract expansion by an inflammatory cell infiltrate, collagen depositions, bile duct infiltrate, intraepithelial cells (nuclear multilayering), pyknotic duct cells, vascular endothelialitis, hepatocellular necrosis, acidophil bodies, microabscesses, mitotic figures, and steatosis). The scoring system for each parameter ranged from 0 to 4 and denoted 0 as normal; 0.5 as focal and rare; 1 as focal and mild; 3 as diffuse and moderate; and 4 as diffuse and severe, as previously published [58,59]. Scores for each parameter were added to provide a total score for each organ; thus, the maximum pathology score for small intestine was 28 and for liver 44. In addition, in small intestine samples, at least 50 crypts per mouse were observed under high-magnification microscopy (100×) to count Paneth cells.

Ex vivo mitochondrial transfer

Mitochondria from human UC-MSCs to murine cells from lymph nodes and spleen was assessed *ex vivo* using a SLE (MRL/MpJ/Fas) and a healthy control (MRL/MpJ) mouse models from The Jackson Laboratory. Animals were kept at specific pathogen-free animal facility of Universidad de los Andes with water and food *ad libitum*, according to international guidelines for animal care and protocols approved by the Institutional Animal Care and Use Committee (ARRIVE Guidelines Animal Research) and approved by the local animal care committee (number CEC201729, June 30, 2017). UC-MSCs were labeled the day before the experiments with MitoTracker Green FM and plated using 48-well plates. Mouse organs were collected and mechanically disrupted for cell extraction in PBS 1× supplemented with 2% FBS and 2 mM EDTA. Co-culture assays were performed at 1:16 MSC:PBMC ratio, and after UC-MSC media were removed, 5×10^5 freshly isolated mouse cells were plated on top of the MSCs. After 24 h, cells were collected, washed with PBS, and stained at 4°C for 20 min using specific antibodies for mouse CD45-PECy7 (#103114, 2:100; BioLegend) and CD3-APC (#100236, 3:100; BioLegend), and labeled with the live/dead near-IR fluorescent dye (as described above). Data were acquired using a FACS Canto II, and MitoT was analyzed with the FlowJo software.

Statistics

Statistical analyses were performed with the aid of Microsoft Excel and GraphPad Prism, and the results were expressed as mean \pm SEM, as indicated in the figure legends. The unpaired, two-tailed, Student's *t*-test was performed to compare two mean values, and $P < 0.05$ was considered statistically significant. For RNA-Seq analysis, transcripts

were considered as statistically DE when presenting a fold change bigger to 1.5 and a *P*-value smaller than 0.05.

Data availability

The datasets (and computer code) produced in this study are available in the following databases: RNA-Seq data: Gene Expression Omnibus GSE140483 (<https://www.ncbi.nlm.nih.gov/geo/query/acc.cgi?acc=GSE140483>).

Expanded View for this article is available online.

Acknowledgements

The authors would like to specially thank Andres Caicedo (Universidad San Francisco de Quito) for scientific assistance regarding the Mitoception protocol, Alex Cabrera, Hector Andrés Ramirez, and Yessia Hidalgo (C4C-Regenero Flow Cytometry Facility) for assistance with flow cytometry and cell sorting, Macarena Ocaña and Claudia Rubí (C4C-Regenero Animal Facility) for technical expertise and assistance in the *in vivo* experiments, Álvaro Elorza (Universidad Andrés Bello) for Seahorse services, and also the members of the C4C laboratory for support and helpful discussion. This work was supported by grants from National Agency for Investigation and Development: ANID (Agencia Nacional de Investigación y Desarrollo) previously branded as the Chilean National Commission for Scientific and Technological Investigation-CONICYT [FONDECYT regular #1170852, FONDAPE-CONICYT #15130011, and PAI-CONICYT #PAI79170021].

Author contributions

FEF, PL-C, ACC, KP-L, and MKh contributed to the conception of the study and experimental design. ACC, AL-G, PL-C, and EP performed the experiments, data analysis, and participated in the acquisition of data. VA-T, MKu, and VM-C performed transcriptome profiling, and whole gene expression and pathway analysis. LFB and RE-V carried out the histopathology analysis, providing images and analysis. RAC and MIO assisted in mouse experiments and data analysis. FEF and MKh prepared the manuscript. All the authors critically revised the manuscript and provided help with interpretation of data. The final manuscript was read and approved by all authors.

Conflict of interest

Maroun Khoury is the CSO of Cells for Cells and Regenero, and Angela Court and Alice LeGatt received stipends from Regenero. The other authors declare that they have no conflict of interest.

References

1. Chang C-H, Curtis JD, Maggi LB Jr, Faubert B, Villarino AV, O'Sullivan D, Huang SC-C, van der Windt GJW, Blagih J, Qiu J *et al* (2013) Posttranscriptional control of T cell effector function by aerobic glycolysis. *Cell* 153: 1239–1251
2. Buck MD, O'Sullivan D, Klein Geltink RII, Curtis JDD, Chang CH, Sanin DEE, Qiu J, Kretz O, Braas D, van der Windt GJJW *et al* (2016) Mitochondrial dynamics controls T cell fate through metabolic programming. *Cell* 166: 63–76
3. Spees JL, Olson SD, Whitney MJ, Prockop DJ (2006) Mitochondrial transfer between cells can rescue aerobic respiration. *Proc Natl Acad Sci USA* 103: 1283–1288

4. Singer NG, Caplan AI (2011) Mesenchymal stem cells: mechanisms of inflammation. *Annu Rev Pathol* 6: 457–478
5. Ahmad T, Mukherjee S, Pattnaik B, Kumar M, Singh S, Rehman R, Tiwari BK, Jha KA, Barhanpurkar AP, Wani MR et al (2014) Miro1 regulates intercellular mitochondrial transport & enhances mesenchymal stem cell rescue efficacy. *EMBO J* 33: 994–1010
6. Jackson MV, Morrison TJ, Doherty DF, McAuley DF, Matthay MA, Kissenpfennig A, O’Kane CM, Krasnodembskaya AD (2016) Mitochondrial transfer via tunneling nanotubes is an important mechanism by which mesenchymal stem cells enhance macrophage phagocytosis in the *in vitro* and *in vivo* models of ARDS. *Stem Cells* 34: 2210–2223
7. Caicedo A, Fritz V, Brondello JM, Ayala M, Dennemont I, Abdellaoui N, De Fraipont F, Moisan A, Prouteau CA, Boukhaddaoui H et al (2015) MitoCeption as a new tool to assess the effects of mesenchymal stem/stromal cell mitochondria on cancer cell metabolism and function. *Sci Rep* 5: 9073
8. Ren G, Zhang L, Zhao X, Xu G, Zhang Y (2008) Mesenchymal stem cell-mediated immunosuppression occurs via concerted action of chemokines and nitric oxide. *Cell Stem Cell* 2: 141–150
9. Smigiel KS, Richards E, Srivastava S, Thomas KR, Dudda JC, Klonowski KD, Campbell DJ (2014) CCR7 provides localized access to IL-2 and defines homeostatically distinct regulatory T cell subsets. *J Exp Med* 211: 121–136
10. Ukena SN, Höpting M, Velaga S, Ivanyi P, Grosse J, Baron U, Ganser A, Franzke A (2011) Isolation strategies of regulatory T cells for clinical trials: phenotype, function, stability, and expansion capacity. *Exp Hematol* 39: 1152–1160
11. Romano M, Tung SL, Smyth LA, Lombardi G (2017) Treg therapy in transplantation: a general overview. *Transpl Int* 30: 745–753
12. Vignais ML, Caicedo A, Brondello JM, Jorgensen C (2017) Cell connections by tunneling nanotubes: effects of mitochondrial trafficking on target cell metabolism, homeostasis, and response to therapy. *Stem Cells Int* 2017: 6917941
13. Chen J, Wang Q, Feng X, Zhang Z, Geng L, Xu T, Wang D, Sun L (2016) Umbilical cord-derived mesenchymal stem cells suppress autophagy of T cells in patients with systemic lupus erythematosus via transfer of mitochondria. *Stem Cells Int* 2016: 4062789
14. Phinney DG, Di Giuseppe M, Njah J, Sala E, Shiva S, St Croix CM, Stolz DB, Watkins SC, Di YP, Leikauf GD et al (2015) Mesenchymal stem cells use extracellular vesicles to outsource mitophagy and shuttle micro-RNAs. *Nat Commun* 6: 8472
15. Wang J, Liu X, Qiu Y, Shi Y, Cai J, Wang B, Wei X, Ke Q, Sui X, Wang Y et al (2018) Cell adhesion-mediated mitochondria transfer contributes to mesenchymal stem cell-induced chemoresistance on T cell acute lymphoblastic leukemia cells. *J Hematol Oncol* 11: 11
16. Hodneland Nilsson LI, Nitschke Pettersen IK, Nikolaisen J, Micklem D, Avsnes Dale H, Vatne Røslund G, Lorens J, Tronstad KJ (2015) A new live-cell reporter strategy to simultaneously monitor mitochondrial biogenesis and morphology. *Sci Rep* 5: 17217
17. Mattiasson G (2004) Flow cytometric analysis of isolated liver mitochondria to detect changes relevant to cell death. *Cytometry* 60: 145–154
18. Cossarizza A, Ceccarelli D, Masini A (1996) Functional heterogeneity of an isolated mitochondrial population revealed by cytofluorometric analysis at the single organelle level. *Exp Cell Res* 222: 84–94
19. Kim MJ, Hwang JW, Yun CK, Lee Y, Choi YS (2018) Delivery of exogenous mitochondria via centrifugation enhances cellular metabolic function. *Sci Rep* 8: 3330
20. van der Windt GJW, Everts B, Chang CH, Curtis JD, Freitas TC, Amiel E, Pearce EJ, Pearce EL (2012) Mitochondrial respiratory capacity is a critical regulator of CD8⁺ T cell memory development. *Immunity* 36: 68–78
21. Pearce EL (2010) Metabolism in T cell activation and differentiation. *Curr Opin Immunol* 22: 314–320
22. Patsoukis N, Bardhan K, Weaver J, Herbel C, Seth P, Li L, Boussiotis VA (2016) The role of metabolic reprogramming in T cell fate and function. *Curr Trends Immunol* 17: 1–12
23. Zhao J, Zhang J, Yu M, Xie Y, Huang Y, Wolff DW, Abel PW, Tu Y (2013) Mitochondrial dynamics regulates migration and invasion of breast cancer cells. *Oncogene* 32: 4814–4824
24. Morlino G, Barreiro O, Baixauli F, Robles-Valero J, Gonzalez-Granado JM, Villa-Belostta R, Cuenca J, Sanchez-Sorzano CO, Veiga E, Martin-Cofreces NB et al (2014) Miro-1 links mitochondria and microtubule dynein motors to control lymphocyte migration and polarity. *Mol Cell Biol* 34: 1412–1426
25. Luz-Crawford P, Kurte M, Bravo-Alegría J, Contreras R, Nova-Lamperti E, Tejedor G, Noël D, Jorgensen C, Figueroa F, Djouad F et al (2013) Mesenchymal stem cells generate a CD4⁺CD25⁺Foxp3⁺ regulatory T cell population during the differentiation process of Th1 and Th17 cells. *Stem Cell Res Ther* 4: 65
26. Khosravi M, Bidmeshkipour A, Cohen JL, Moravej A, Hojjat-Assari S, Naseirian S, Karimi MH (2018) Induction of CD4⁺CD25⁺FOXP3⁺ regulatory T cells by mesenchymal stem cells is associated with modulation of ubiquitination factors and TSDR demethylation. *Stem Cell Res Ther* 9: 273
27. Cahill EF, Tobin LM, Carty F, Mahon BP, English K (2015) Jagged-1 is required for the expansion of CD4⁺CD25⁺FoxP3⁺ regulatory T cells and tolerogenic dendritic cells by murine mesenchymal stromal cells. *Stem Cell Res Ther* 6: 19
28. Khosravi M, Karimi MH, Hossein Aghdaie M, Kalani M, Naseirian S, Bidmeshkipour A (2017) Mesenchymal stem cells can induce regulatory T cells via modulating miR-126a but not miR-10a. *Gene* 627: 327–336
29. Tyrakis PA, Palazon A, Macias D, Lee KL, Phan AT, Veliça P, You J, Chia GS, Sim J, Doedens A et al (2016) S-2-hydroxyglutarate regulates CD8⁺ T-lymphocyte fate. *Nature* 540: 236–241
30. Cardamone MD, Tanasa B, Cederquist CT, Huang J, Mahdavian K, Li W, Rosenfeld MG, Liesa M, Perissi V (2018) Mitochondrial retrograde signaling in mammals is mediated by the transcriptional cofactor GPS2 via direct mitochondria-to-nucleus translocation. *Mol Cell* 69: 757–772.e7
31. Lentucci C, Belkina AC, Cederquist CT, Chan M, Johnson HE, Prasad S, Lopacinski A, Nikolajczyk BS, Monti S, Snyder-Cappione J et al (2017) Inhibition of Ubc13-mediated ubiquitination by GPS2 regulates multiple stages of B cell development. *J Biol Chem* 292: 2754–2772
32. Ito T, Hanabuchi S, Wang YH, Park WR, Arima K, Bover L, Qin FFX, Gilliet M, Liu YJ (2008) Two functional subsets of FOXP3⁺ regulatory T cells in human thymus and periphery. *Immunity* 28: 870–880
33. Zheng J, Chan PL, Liu Y, Qin G, Xiang Z, Lam KT, Lewis DB, Lau YL, Tu W (2013) ICOS regulates the generation and function of human CD4⁺ Treg in a CTLA-4 dependent manner. *PLoS ONE* 8: e82203
34. Vocanson M, Rozieres A, Hennino A, Poyet G, Gaillard V, Renaudineau S, Achachi A, Benetiere J, Kaiserlian D, Dubois B et al (2010) Inducible costimulator (ICOS) is a marker for highly suppressive antigen-specific T cells sharing features of TH17/TH1 and regulatory T cells. *J Allergy Clin Immunol* 126: 280–289
35. Zeng H, Yang K, Cloer C, Neale G, Vogel P, Chi H (2013) MTORC1 couples immune signals and metabolic programming to establish Treg-cell function. *Nature* 499: 485–490

36. Liakou CI, Kamat A, Tang DN, Chen H, Sun J, Troncoso P, Logothetis C, Sharma P (2008) CTLA-4 blockade increases IFN-producing CD4⁺ ICOShi cells to shift the ratio of effector to regulatory T cells in cancer patients. *Proc Natl Acad Sci USA* 105: 14987–14992
37. Redpath SA, van der Werf N, Cervera AM, Macdonald AS, Gray D, Maizels RM, Taylor MD (2013) ICOS controls Foxp3⁺ regulatory T-cell expansion, maintenance and IL-10 production during helminth infection. *Eur J Immunol* 43: 705–715
38. Schneider MA, Meingassner JG, Lipp M, Moore HD, Rot A (2007) CCR7 is required for the *in vivo* function of CD4⁺ CD25⁺ regulatory T cells. *J Exp Med* 204: 735–745
39. Campbell JJ, Murphy KE, Kunkel EJ, Brightling CE, Soler D, Shen Z, Boisvert J, Greenberg HB, Vierra MA, Goodman SB et al (2001) CCR7 Expression and memory T cell diversity in humans. *J Immunol* 166: 877–884
40. Menning A, Höpken UE, Siegmund K, Lipp M, Hamann A, Huenn J (2007) Distinctive role of CCR7 in migration and functional activity of naive- and effector/memory-like Treg subsets. *Eur J Immunol* 37: 1575–1583
41. Taylor PA, Lees CJ, Blazar BR (2002) The infusion of *ex vivo* activated and expanded CD4⁺CD25⁺ immune regulatory cells inhibits graft-versus-host disease lethality. *Blood* 99: 3493–3499
42. Rezvani K, Mielke S, Ahmadzadeh M, Kilical Y, Savani BN, Zeilich J, Keyvanfar K, Montero A, Hensel N, Kurlander R et al (2006) High donor FOXP3-positive regulatory T-cell (Treg) content is associated with a low risk of GVHD following HLA-matched allogeneic SCT. *Blood* 108: 1291–1297
43. Ramlal R, Hildebrandt GC (2017) Advances in the use of regulatory T-cells for the prevention and therapy of graft-vs.-host disease. *Biomedicine* 5: 23
44. Eriguchi Y, Takashima S, Oka H, Shimoji S, Nakamura K, Uryu H, Shimoda S, Iwasaki H, Shimono N, Ayabe T et al (2012) Graft-versus-host disease disrupts intestinal microbial ecology by inhibiting Paneth cell production of α -defensins. *Blood* 120: 223–231
45. Levine JE, Huber E, Hammer STG, Harris AC, Greenson JK, Braun TM, Ferrara JLM, Holler E (2013) Low Paneth cell numbers at onset of gastrointestinal graft-versus-host disease identify patients at high risk for nonrelapse mortality. *Blood* 122: 1505–1509
46. Alcayaga-Miranda F, Cuenca J, Luz-Crawford P, Aguila-Díaz C, Fernandez A, Figueroa FE, Khoury M (2015) Characterization of menstrual stem cells: angiogenic effect, migration and hematopoietic stem cell support in comparison with bone marrow mesenchymal stem cells. *Stem Cell Res Ther* 6: 32
47. González PL, Carvajal C, Cuenca J, Alcayaga-Miranda F, Figueroa FE, Bartolucci J, Salazar-Aravena L, Khoury M (2015) Chorion mesenchymal stem cells show superior differentiation, immunosuppressive, and angiogenic potentials in comparison with haploidentical maternal placental cells. *Stem Cells Transl Med* 4: 1109–1121
48. Luz-Crawford P, Torres MJ, Noël D, Fernandez A, Toupet K, Alcayaga-Miranda F, Tejedor G, Jorgensen C, Illanes SE, Figueroa FE et al (2016) The immunosuppressive signature of menstrual blood mesenchymal stem cells entails opposite effects on experimental arthritis and graft versus host diseases. *Stem Cells* 34: 456–469
49. Cuenca J, Le-Gatt A, Castillo V, Belletti J, Díaz M, Kurte GM, Gonzalez PL, Alcayaga-Miranda F, Schuh CMAP, Ezquer F et al (2018) The reparative abilities of menstrual stem cells modulate the wound matrix signals and improve cutaneous regeneration. *Front Physiol* 9: 464
50. Bolger AM, Lohse M, Usadel B (2014) Trimmomatic: a flexible trimmer for Illumina sequence data. *Bioinformatics* 30: 2114–2120
51. Hubbard T (2002) The Ensembl genome database project. *Nucleic Acids Res* 30: 38–41
52. Kim D, Langmead B, Salzberg SL (2015) HISAT: a fast spliced aligner with low memory requirements. *Nat Methods* 12: 357–360
53. Trapnell C, Roberts A, Goff L, Pertea G, Kim D, Kelley DR, Pimentel H, Salzberg SL, Rinn JL, Pachter L (2012) Differential gene and transcript expression analysis of RNA-seq experiments with TopHat and Cufflinks. *Nat Protoc* 7: 562–578
54. Kuleshov MV, Jones MR, Rouillard AD, Fernandez NF, Duan Q, Wang Z, Koplev S, Jenkins SL, Jagodnik KM, Lachmann A et al (2016) Enrichr: a comprehensive gene set enrichment analysis web server 2016 update. *Nucleic Acids Res* 44(W1): W90–W97
55. Liberzon A, Subramanian A, Pinchback R, Thorvaldsdóttir H, Tamayo P, Mesirov JP (2011) Molecular signatures database (MSigDB) 3.0. *Bioinformatics* 27: 1739–1740
56. Cooke KR, Kobzik L, Martin TR, Brewer J, Delmonte J, Crawford JM, Ferrara JL (1996) An experimental model of idiopathic pneumonia syndrome after bone marrow transplantation: I. The roles of minor H antigens and endotoxin. *Blood* 88: 3230–3239
57. Cooke KR, Krenger W, Hill G, Martin TR, Kobzik L, Brewer J, Simmons R, Crawford JM, van den Brink MR, Ferrara JL (1998) Host reactive donor T cells are associated with lung injury after experimental allogeneic bone marrow transplantation. *Blood* 92: 2571–2580
58. Hill GR, Cooke KR, Teshima T, Crawford JM, Keith JC, Brinson YS, Bungard D, Ferrara JLM (1998) Interleukin-11 promotes T cell polarization and prevents acute graft-versus-host disease after allogeneic bone marrow transplantation. *J Clin Invest* 102: 115–123
59. Hill GR, Crawford JM, Cooke KR, Brinson YS, Pan L, Ferrara JL (1997) Total body irradiation and acute graft-versus-host disease: the role of gastrointestinal damage and inflammatory cytokines. *Blood* 90: 3204–3213
60. Teshima T, Ordemann R, Reddy P, Gagin S, Liu C, Cooke KR, Ferrara JLM (2002) Acute graft-versus-host disease does not require alloantigen expression on host epithelium. *Nat Med* 8: 575–581